https://doi.org/10.5194/egusphere-2026-4040
Preprint. Discussion started: 16 July 2026

Use of a GNSS-PRO forward operator for the evaluation of global and km-scale NWP models

Antía Paz[1,2,3], Clotilde Augros[4], Dominique Raspaud[4], Mary Borderies[4], Ramon Padullés[1,2], Estel Cardellach[1,2], and Cloé David[4]

[1]Institute of Space Sciences-Consejo Superior de Investigaciones Científicas (ICE-CSIC), Barcelona, Spain
[2]Institute of Space Studies of Catalonia (IEEC), Barcelona, Spain
[3]Facultat de Física, Universitat de Barcelona (UB), Carrer de Martí i Franquès, 1-11, 08028 Barcelona, Spain
[4]Météo-France, CNRS, Univ. Toulouse, CNRM, Toulouse, France

Correspondence: Antía Paz (a.paz@csic.es)

Abstract. A new formulation for a Polarimetric Radio Occultation (PRO) forward operator was recently developed and evaluated with the Weather Research and Forecasting (WRF) model and the European Center for Medium-Range Weather Forecasts (ECMWF) Integrated Forecasting System (IFS), representing a promising step toward the assimilation of PRO observations in numerical weather prediction (NWP) systems and a novel tool for evaluating frozen-hydrometeor microphysical parameterizations. In this study, the operator is applied for the first time across two operational Météo-France systems: the convection-permitting Applications of Research to Operations at Mesoscale (AROME) model and its overseas configuration, AROME-OM, and the global Action de Recherche Petite Échelle Grande Échelle (ARPEGE) model. Twenty-seven PRO occultations, each co-located with simulations from both AROME/AROME-OM and ARPEGE, are analyzed, spanning metropolitan France and the French overseas territories (Antilles, Southwest Indian Ocean, French Polynesia and New Caledonia) across both mid-latitude convective and stratiform precipitation, and tropical convective regimes. The PRO observations are first cross-checked against the ARAMIS ground-based radar observations over metropolitan France, providing an observation-only reference independent of either forward operator. For all AROME cases, the PRO operator is then systematically compared with the polarimetric radar forward operator (operadar) driven by the same AROME fields. The PRO operator globally achieves a better agreement with the observations than operadar across all regions, mainly because of its optimized nature, although a remarkably good agreement is found between the two operators and the observations over the metropolitan France domain. The PRO operator further serves as a diagnostic of how each NWP model partitions frozen water content among its prognostic species, and help identify the species that are the most difficult to accurately simulate with operadar (snow and wet graupel). These findings establish the PRO operator as a versatile multi-model diagnostic for frozen-hydrometeor microphysics and underline the operational potential of PRO observations as a complement to ground-based polarimetric radar networks, especially over seas.

Keywords: Polarimetric Radio Occultations; forward operator; operadar; AROME; ARPEGE

https://doi.org/10.5194/egusphere-2026-4040
Preprint. Discussion started: 16 July 2026

1 Introduction

Accurately representing precipitation processes in Numerical Weather Prediction (NWP) remains one of the central challenges in atmospheric modeling. The microphysical processes that govern the formation, growth, and fallout of hydrometeors occur at scales far below the resolution of operational NWP systems and must therefore be described through simplified parameterizations that rely on assumptions about the shape, particle size distribution, and density of the particles (Morrison et al., 2020). Improving these parameterizations requires observational constraints that are sensitive not only to the thermodynamic state of the atmosphere but also to the presence, phase, and size distribution, quantities which require a diverse observational network to be properly constrained (Geer, 2021).

The Global Navigation Satellite System (GNSS) Radio Occultation (RO) technique is a well-established remote sensing method that provides vertically resolved profiles of atmospheric refractivity from which thermodynamic variables such as temperature, pressure, or water vapor pressure can be retrieved with high vertical resolution, global coverage, and all-weather capability (e.g., Kursinski et al., 1997). The technique is based on the reception by a Low Earth Orbit (LEO) satellite of GNSS signals that have traversed the atmosphere and undergone bending due to vertical gradients in the refractive index. Owing to their accuracy and global coverage, RO-derived products have been demonstrated to have an important impact on model forecast (e.g. Healy et al., 2005; Cucurull et al., 2007; Ruston and Healy, 2021). More recently, it has been shown that assimilating a very large number of RO data significantly improves the forecast skill, without any saturation effect (Bowler and Lewis, 2026). However, conventional RO observations rely on the reception of Right Hand Circularly Polarized (RHCP) signals and are therefore insensitive to the polarimetric properties of the medium, providing no direct information on condensed variables.

The Polarimetric Radio Occultation (PRO) technique extends the conventional RO approach by measuring the signal in two orthogonal linear polarizations, horizontal (H) and vertical (V). The phase difference between these two components defines the differential phase shift ($\Delta\Phi\Delta\Phi$), which is sensitive to the presence of non-spherical and preferentially oriented hydrometeors. When GNSS signals propagate through precipitation systems containing oblate or horizontally aligned particles, differential propagation effects arise, leading to a positive $\Delta\Phi\Delta\Phi$ (Cardellach et al., 2014, 2019). PRO therefore provides, from the same measurement geometry, both the thermodynamic profile information of conventional RO and a novel polarimetric sensitivity to the structure of precipitation along the path, making it a unique observational tool for constraining in a consistent way hydrometeor and thermodynamic properties in NWP. This sensitivity to hydrometeors was first confirmed in practice through observations from the PAZ satellite, the first mission to carry a PRO payload in orbit (Cardellach et al., 2019). These early observations revealed unexpectedly large signals from frozen particles (Padullés et al., 2021), in contrast to the pre-launch design strategies, which had focused primarily on rain rate retrievals (Cardellach et al., 2018). Since then, efforts have shifted from deriving standalone geophysical products toward the broader exploitation of the PRO observable itself.

Exploiting the polarimetric sensitivity of PRO observable in an NWP context requires a forward operator that maps the model-predicted microphysical state to the observed $\Delta\Phi$ signal. Hotta et al. (2024) tested an operator configuration at ECMWF in Atmospheric River (AR) and Tropical Cyclone (TC) conditions, and a new formulation of the forward operator was subse-

https://doi.org/10.5194/egusphere-2026-4040
Preprint. Discussion started: 16 July 2026

quently developed and evaluated in Padullés et al. (2025a); Paz et al. (2025, 2026), in which hydrometeor-specific scattering efficiency parameters, coefficients that relate the water content of each frozen hydrometeor species to its contribution to the differential phase shift, are retrieved by Bayesian inversion. The availability of such an operator opens the door to using PRO observations as a diagnostic and, potentially, an assimilation constraint on the frozen part of the modelled hydrometeor column.

The potential of PRO for informing the microphysical representation in NWP models was first proposed by Murphy Jr et al. (2019). Subsequent work showed that the simulation of PRO observations is highly sensitive to the microphysics scheme employed and to the frozen particle habits assumed within it, with applications reported for the WRF model (Chen et al., 2025; Paz et al., 2025) and, more recently, the ECMWF Integrated Forecasting System (IFS) (Paz et al., 2026). These studies indicate that PRO observations carry sufficient information content on snow and, to a lesser extent, on other frozen species to constrain their representation in NWP forecasts, and that they could jointly constrain the thermodynamic and the condensed water fields in global NWP systems (Paz et al., 2026). As a globally distributed, all-weather constraint on frozen hydrometeors, PRO would complement the existing satellite observing systems that carry microphysical information over both land and ocean, such as for instance spaceborne radars (Fielding and Janisková, 2020; Ikuta et al., 2021; Mangla et al., 2025), lidars (Fielding and Janisková, 2020), radiances (Geer et al., 2018), and lightning observations (Combarnous et al., 2024), each of which is sensitive to a different part of the hydrometeor spectrum.

The present study applies this forward operator framework for the first time across two operational Météo-France NWP systems: the convection-permitting AROME limited-area model (Brousseau et al., 2016) and its overseas configuration AROME-OM (Faure et al., 2020), both employing the ICE3 bulk microphysics scheme (Pinty and Jabouille, 1998); and the global ARPEGE NWP model (Bouyssel et al., 2022), which uses a different set of prognostic hydrometeors. A total of 27 PRO occultations co-located with these simulations are analyzed, spanning metropolitan France and four French overseas territories (Antilles, Southwest Indian Ocean, Polynesia and New Caledonia, hereafter referred to as Antilles, La Réunion, Polynesia and New Caledonia), and providing a geographically diverse ensemble that covers both mid-latitude stratiform and tropical convective precipitation regimes.

Two complementary intercomparisons are presented. First, the PRO observation itself is cross-checked against a $\Delta\Phi$ derived from the ARAMIS ground-based polarimetric radar network over metropolitan France, providing an independent observational reference. Building on this, at the operator level, the PRO operator is systematically compared against the Observation oPErator for polarimetric RADAR (operadar, Augros et al., 2016; David et al., 2025), which is driven by the same AROME and AROME-OM fields, allowing the contrasting sensitivities of the two operators to be quantified species by species. The PRO operator is then used as a fixed diagnostic to compare the AROME and ARPEGE retrieved scattering efficiencies, enabling an assessment of the operator's applicability across a regional convection-permitting and a global NWP system, and in tropical regions where ground-based radar coverage is sparse or absent.

The remainder of this article is structured as follows. Section 2 describes the datasets and methodology, including the forward operators and the Bayesian inversion framework. Section 3 presents the independent cross-check against ARAMIS and the operator-level intercomparison between the PRO operator and the ground-based polarimetric radar forward operator. Section 4 presents the model-level analysis with the AROME / AROME-OM and ARPEGE retrievals. Section 5 synthesises

https://doi.org/10.5194/egusphere-2026-4040
Preprint. Discussion started: 16 July 2026

the implications of both intercomparisons, situates them relatively to previous WRF- and IFS-based studies, and identifies limitations and future work. Section 6 summarizes the main conclusions.

2 Data and methodology

2.1 Observations

2.1.1 GNSS-PRO observations

PRO observations are drawn from two sources. The PAZ satellite, a Spanish LEO mission carrying the first PRO payload, the Radio Occultation and Heavy Precipitation (ROHP) experiment (Cardellach et al., 2014, 2019), has been delivering calibrated observations since May 2018. These are complemented by observations from the Spire nanosatellite constellation (Talpe et al., 2025; Padullés et al., 2025a).

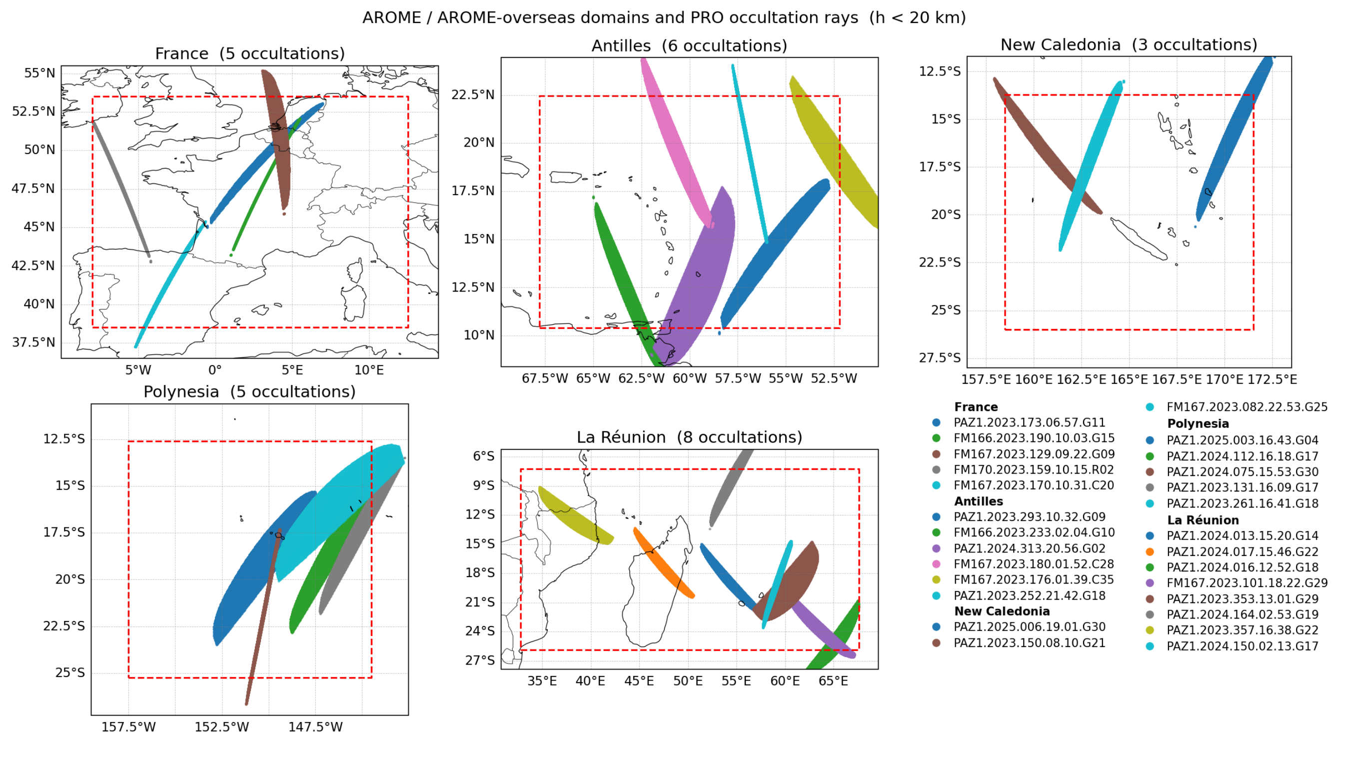

Figure 1. AROME and AROME-OM model domains (red dashed rectangles) and PRO occultation rays below 20 km (coloured points) for each of the five geographical regions analysed in this study: metropolitan France, the Antilles, Polynesia, New Caledonia, and Reunion. Each colour identifies one occultation, with the corresponding case identifier given in the legend (bottom right)

Each observation file contains a vertical profile of $\Delta\Phi$ expressed in units of length (mm) as a function of the tangent height of the corresponding ray (Padullés et al., 2024b). The tangent height is the minimum altitude reached by each ray. Although $\Delta\Phi$ is

https://doi.org/10.5194/egusphere-2026-4040
Preprint. Discussion started: 16 July 2026

attributed to the tangent height, hydrometeors along the entire ray path contribute to the signal, making $\Delta\Phi$ an inherently path-integrated observable. The files also contain three-dimensional ray trajectories derived through ray tracing. Each observation is uniquely identified by an occultation identifier, hereafter referred to as a *roid*.

The dataset comprises 27 occultations (see Tables A1) events selected on the basis of having a substantial $\Delta\Phi$ signal. The different observations and geographical regions can be seen in Figure 1. The cases are distributed across five geographical regions: metropolitan France (5 cases), the Antilles (6 cases), Reunion Island (8 cases), Polynesia (5 cases), and New Caledonia (3 cases).

2.1.2 Ground-based Polarimetric Radar observations

Ground-based K_{dp} observations from the Application Radar à la Météorologie Infra-Synoptique (ARAMIS) polarimetric weather radar network are used for comparison with the GNSS-PRO observations, following the methodology by Paz et al. (2024). For each radar, K_{dp} fields are first retrieved from the operational Serval radar processing chain (Figueras i Ventura et al., 2012) in the native radar geometry, i.e., polar coordinates for each elevation angle within the selected 5 min acquisition period. Since the ground-based radars used for the comparison operate at C-band, the estimated K_{dp} is then converted to an equivalent L-band value according to

$$K_{dp_L} = K_{dp_C} \times \frac{\lambda_C}{\lambda_L}, \tag{1}$$

where $\lambda_C = 5.32$ cm and $\lambda_L = 19.04$ cm are the C- and L-band wavelengths, respectively. This conversion is justified by the fact that, under the Rayleigh scattering approximation, K_{dp} is inversely proportional to the radar wavelength (see Eq. 5.1 of Ryzhkov and Zrnić, 2019).

The L-band-equivalent K_{dp} observations from all elevation angles and all ARAMIS radars surrounding each GNSS-PRO radio occultation are subsequently merged into a three-dimensional composite using the open-source Py-ART package (Python ARM Radar Toolkit, Helmus and Collis, 2016). The compositing procedure follows exactly the methodology described in Section 3.1 of David et al. (2025).

A simulated $\Delta\Phi_{\text{aramis}}$ was then derived from the 3D K_{dp} grid, for the two cases over France that were best covered by the radar network, by integrating K_{dp} along the GNSS ray path (as done in Paz et al., 2024).

2.2 Models

2.2.1 AROME and AROME-OM

This study uses forecasts from the Application of Research to Operations at Mesoscale (AROME-France) model, the operational limited-area NWP system of Météo-France (Seity et al., 2011; Brousseau et al., 2016). Operational at Météo-France since 2008, AROME has been built using the physical parametrization of Méso-NH (Lafore et al., 1998; Lac et al., 2018) and the dynamical part is a fine-scale adaptation of the ALADIN model (Bubnová et al., 1995). The AROME-France system covers

https://doi.org/10.5194/egusphere-2026-4040
Preprint. Discussion started: 16 July 2026

metropolitan France and its neighbouring countries (see top left panel in Figure 1). The lateral boundary conditions are defined using forecasts from the global NWP model ARPEGE of Météo-France (Bouyssel et al., 2022). In the version of AROME used in this study, AROME-France has a 3DVar data assimilation system to upgrade the initial conditions every 1 hour.

In addition, Météo-France runs operationally five NWP configurations in the tropical belt. They are based on AROME-France and are called the AROME-OM systems (Faure et al., 2020). Contrary to AROME-France, these overseas AROME configurations use IFS forecasts from ECMWF for both initialization and lateral forcing.

Both AROME-France and AROME overveas models are spectral and non-hydrostatic. They run at a horizontal resolution of approximately 1.3 km, with 90 vertical levels. The cloud and precipitation microphysics are represented by the ICE3 one-moment bulk scheme (Pinty and Jabouille, 1998), which prognoses five hydrometeor condensate categories: cloud water, rain, pristine ice, snow, and graupel, each characterized by a prescribed mass-size relationship and a modified gamma particle size distribution.

2.2.2 ARPEGE

In addition to AROME, model forecasted fields from the ARPEGE global NWP model are also used (Bouyssel et al., 2022). ARPEGE is the operational global NWP model of Météo-France, with 105 vertical levels. In ARPEGE, the spectral truncation is TL1798 and it has a stretch and titled grid, providing a horizontal resolution of approximately 5 km over Europe and about 24 km near the antipodes (e.g. New Zealand). The model is characterized by 105 vertical levels, from ∼10m above the ground to model top at 0.1 hPa (∼70 km). ARPEGE makes use of 6 hydrometeor types to represent clouds and precipitation. Four of them are prognostic variables (stratiform snow, stratiform rain, cloud liquid water and cloud ice). Their evolution is governed by the Lopez (2002) microphysical scheme. The remaining two hydrometeors species (convective snow and convective rain) of ARPEGE are diagnosed variables and governed by the deep convective scheme of Tiedtke (1989).

2.3 PRO forward operator

The PRO forward operator used in this analysis follows the formulation introduced by Padullés et al. (2025c) and previously evaluated with the WRF (Paz et al., 2025) and IFS (Paz et al., 2026) models. It relates the model-resolved hydrometeor water-content profiles along the PRO ray path to the observable $\Delta\Phi$ through the specific differential phase K_{dp}, the polarimetric quantity whose path integral along the ray gives $\Delta\Phi$. At the L-band frequencies, K_{dp} can be expressed in terms of water content (WC) with a linear relation, for frozen hydrometeors, (Padullés et al., 2025c). The operator is written as the sum of a liquid and a frozen contribution,

$$K_{\mathrm{dp}} = K_{\mathrm{dp}}^{\mathrm{liquid}} + K_{\mathrm{dp}}^{\mathrm{frozen}}, \tag{2}$$

For liquid hydrometeors, the relation between K_{dp} and WC adopts the empirical power law of Bringi and Chandrasekar (2001), well-known in radar literature.

https://doi.org/10.5194/egusphere-2026-4040
Preprint. Discussion started: 16 July 2026

$$K_{\mathrm{dp}}^{\mathrm{liquid}} = A \cdot WC_{\mathrm{liquid}}^{B}, \tag{3}$$

with the fixed coefficients $A = 0.13$ and $B = 1.314$.

For frozen hydrometeors, instead of adopting prescribed coefficients, the operator assigns to each frozen species i a per-unit-mass scattering efficiency x_i, in $\mathrm{mm}\,(\mathrm{kg\,m^{-2}})^{-1}$, and writes the frozen contribution as a linear sum,

$$K_{\mathrm{dp}}^{\mathrm{frozen}} = \sum_{i \in \mathrm{fhy}} x_i \cdot WC_i. \tag{4}$$

Physically, x_i measures how efficiently one unit of water content of species i produces differential phase shift at L-band in RO propagation geometry: it absorbs the joint dependence of K_{dp} on particle habit, density, preferential orientation and prescribed size distribution into a single effective per-species parameter. Aspheric, horizontally-aligned frozen particles such as large snow aggregates, dendrites or plate-like crystals carry large x_i, whereas nearly spheroidal or randomly oriented particles carry small ones. In contrast to the fixed liquid coefficients, the x_i are not prescribed a priori but retrieved from PRO observations through Bayesian inversion (Sec. 2.3.1).

Combining the two contributions, the complete operator reads

$$K_{\mathrm{dp}} = \sum_{i \in \mathrm{lhy}} A \cdot WC_i^{B} + \sum_{i \in \mathrm{fhy}} x_i \cdot WC_i, \tag{5}$$

where lhy and fhy denote the model's liquid and frozen hydrometeor species. The simulated $\Delta\Phi$ is obtained by integrating K_{dp} along the bent GNSS ray path,

$$\Delta\Phi = \int_{L} K_{\mathrm{dp}}(l)\,\mathrm{d}l. \tag{6}$$

where l is the along-path coordinate and L denotes the full bent ray path traced through the model fields, obtained via ray tracing as described in Section 2.1.1.

2.3.1 Bayesian inversion

The scattering efficiency parameters x_i are retrieved by minimizing the weighted least-squares residual between observed and simulated $\Delta\Phi$, following the same agreement-weighted optimization framework introduced in Paz et al. (2026). For a single occultation, the observation vector $\mathbf{y}$ (observed $\Delta\Phi$ minus the liquid contribution) is expressed as

$$\mathbf{y} = \mathbf{A} \cdot \mathbf{x} + \boldsymbol{\epsilon} \tag{7}$$

https://doi.org/10.5194/egusphere-2026-4040
Preprint. Discussion started: 16 July 2026

where $\mathbf{A}$ contains the along-ray integrated water content profiles and $\mathbf{x}$ is the parameter vector. The optimal solution minimizes:

$$J(\mathbf{x}) = (\mathbf{y} - \mathbf{A}\cdot\mathbf{x})^T\mathbf{R}^{-1}(\mathbf{y} - \mathbf{A}\cdot\mathbf{x}) \tag{8}$$

where $\mathbf{R} = \mathrm{diag}(\sigma_i^2)$ is the diagonal observation error covariance matrix. The uncertainty σ_i is defined as:

$$\sigma_i = \frac{\mathrm{SD}_i}{\sqrt{50}} \tag{9}$$

where SD_i is the standard deviation of $\Delta\Phi$ at 50 Hz over one-second intervals (Padullés et al., 2024b).

The retrieval is performed globally by stacking all $N = 27$ occultations into a single linear system,

$$\mathbf{y}_{\mathrm{all}} = \begin{bmatrix}\mathbf{y}_1\\ \vdots \\ \mathbf{y}_N\end{bmatrix}, \qquad \mathbf{A}_{\mathrm{all}} = \begin{bmatrix}\mathbf{A}_1\\ \vdots \\ \mathbf{A}_N\end{bmatrix} \tag{10}$$

To prevent occultations with intrinsically poor individual fits from dominating the joint solution, each case is down-weighted by its own goodness fit, as in Paz et al. (2026). A preliminary per-case inversion yields a reduced chi-squared $\chi^2_{\nu,m}$ for case m, and its nominal uncertainty is rescaled to an effective uncertainty,

$$\sigma^{\mathrm{eff}}_{m,i} = \sigma_{m,i}\sqrt{\chi^2_{\nu,m}} \tag{11}$$

before assembling the global $\mathbf{R}$ in Eq. 8. Cases with $\chi^2_{\nu,m} \gg 1$ are therefore assigned effectively inflated uncertainties and contribute less to the global retrieval. The Maximum a Posteriori (MAP) solution is computed with a bounded trust region linear least-squares solver (*scipy.optimize.lsq_linear*), with each x_i constrained to a prescribed lower bound of 10^{-3} mm (kg $m^{-2})^{-1}$ rather than zero, so that the solver retains a small but strictly positive sensitivity for every species and species with negligible support in the observations saturate at this bound instead of vanishing. The $sigma$ parameter uncertainties are read from the diagonal of the Laplace posterior covariance $\mathbf{S}_x = (\mathbf{A}_{\mathrm{all}}^\top\mathbf{R}^{-1}\mathbf{A}_{\mathrm{all}})^{-1}$.

2.4 Operadar

The operadar is a polarimetric radar forward operator developed at Météo-France (Augros et al., 2016; David et al., 2025) that simulates polarimetric variables from AROME model fields using T-matrix scattering calculations (Mishchenko and Travis, 1994). For this study, the simulations were adapted to the L-band frequency. In operadar, the forward- and back-scattering coefficients are computed for each diameter of each AROME hydrometeor specie (cloud water, rain, snow, graupel, pristine ice) with the mass-size relationships given by the model microphysics scheme (ICE3 in this study). The coefficients are then integrated over the particle size distribution also defined in the microphysics scheme.

https://doi.org/10.5194/egusphere-2026-4040
Preprint. Discussion started: 16 July 2026

A key feature of operadar is its treatment of the melting layer. As no wet fraction is prescribed within the microphysics scheme, operadar considers the graupel specie as being wet as soon as it coexists with rain. A wet fraction F_w is diagnosed as the ratio between the rain content M_r and the sum of rain plus the graupel content M_g:

$$F_w = \frac{M_r}{M_r + M_g} \tag{12}$$

This wet fraction is then employed in the computation of the dielectric constant of the wet graupel as detailed in Appendix B of David et al. (2025). The hydrometeor contents used in operadar, including the diagnosed wet graupel content are also used as input to the PRO forward operator, ensuring a consistent comparison between the two operators.

In this study, a recently improved configuration of operadar was employed, as described in Chapter 4 of David (2026). In this configuration, all hydrometeor species are assigned a canting angle distribution, with standard deviations of 10° for rain and pristine ice, and 40° for graupel and snow. The axis ratios of snow and pristine ice are assumed to be constant, with values of 0.6 and 0.2, respectively, in the radar geometry.

2.5 Definition of metrics

The agreement between the observed differential phase shift $\Delta\Phi$ and the simulated by the forward operator is quantified through three complementary statistical metrics: the root mean square error (RMSE), the bias, and the reduced chi-squared (χ^2_{red}). The RMSE measures the overall magnitude of the residuals between simulation and observation, the bias captures any systematic offset between the two, and the reduced chi-squared normalizes the residuals by the observational uncertainty σ_i defined in Equation 11, taking a value close to unity when the residuals are consistent with the assumed measurement noise and values much greater than unity when the model–observation discrepancy exceeds what the observation error alone can explain. For a profile with N vertical levels, y_i the observation at level i and y_i^{sim} the corresponding simulated value, the three metrics are defined as:

$$\text{RMSE} = \sqrt{\frac{1}{N}\sum_{i=1}^{N}\left(y_i - y_i^{\text{sim}}\right)^2} \tag{13}$$

$$\text{Bias} = \frac{1}{N}\sum_{i=1}^{N}\left(y_i - y_i^{\text{sim}}\right) \tag{14}$$

$$\chi^2_{\text{red}} = \frac{1}{N}\sum_{i=1}^{N}\left(\frac{y_i - y_i^{\text{sim}}}{\sigma_i}\right)^2 \tag{15}$$

3 Intercomparison of PRO and operadar

This section evaluates the PRO and operadar forward operators against the PRO observations introduced in section 2. Both operators are driven by the same AROME and AROME-OM hydrometeor fields, so that any difference between their simulated

https://doi.org/10.5194/egusphere-2026-4040
Preprint. Discussion started: 16 July 2026

$\Delta\Phi$ profiles reflects the contrasting physical assumptions of the two operators. The comparison is shown in four steps: we first present an independent cross-check of the PRO observations against ground-based polarimetric radar observations over metropolitan France (subsection 3.1), which provides an observational reference; we then turn to the systematic comparison of the PRO operator and operadar across the full 27 cases (subsection 3.2); and the physical mechanism behind the systematic differences between the two operators is then examined by decomposing the simulated $\Delta\Phi$ (subsection 3.3) across the different hydrometeors.

3.1 Comparison over France with ground-based weather radars

As detailed in subsubsection 2.1.2, a simulated $\Delta\Phi_{\mathrm{aramis}}$ was derived from ground-based radar K_{dp} observations, for the two cases over France that were best covered by the radar network. Figure 2 shows, for one of the two cases, the co-location geometry (left), the observed reflectivity from the ARAMIS network (middle) and the corresponding AROME-simulated reflectivity (right). The PRO ray trajectories below 20 km (grey shading, all three panels) and the occultation point (black dot) are overlaid on the reflectivity panels to indicate which part of the precipitation field is sampled by the PRO signal. In the left panel, the 150 km coverage circles of the Météo-France radars whose fields of view intersect the occultation footprint are shown in colour, indicating that the PRO ray traverses a region that is well sampled by at least one polarimetric radar at every point along its projection. The middle panel displays the column-maximum reflectivity obtained from the 3D reflectivity grid derived using Py-Art applied to the radars displayed in the left panel, at the closest acquisition time. The right panel shows the column-maximum reflectivity simulated by operadar from the AROME forecast at the closest valid time, both on the same dBZ colour scale to facilitate direct comparison.

Beyond providing the geometrical context for the comparison, the two reflectivity panels show that AROME reproduces the broad structure of the precipitating system intersected by the PRO ray. The model captures the elongated band of high reflectivity oriented roughly along the ray path, the position of the most intense cells in the immediate vicinity of the occultation point and the general extent of the precipitation field over the northern half of France. The observed and simulated peak reflectivities reach comparable values of ~50–55 dBZ. The AROME field is, however, more spatially fragmented than the observation, with weak-reflectivity precipitation extending further from the main band. This qualitative agreement at the column-integrated level provides a baseline for interpreting the $\Delta\Phi$ comparison that follows: the AROME hydrometeor fields sampled along the PRO ray are at least broadly consistent with the actual precipitation structure observed by ARAMIS.

Figure 3 compares $\Delta\Phi_{\mathrm{aramis}}$ with the PRO observation for the two cases considered over France. The two profiles exhibit a consistent vertical structure, with both showing $\Delta\Phi$ increases around the same principal peaks. The radar-derived profiles are noisier than the PRO ones. Although the radar K_{dp} values are smoothed in the 3D grid interpolation and after the integration along the ray path (see subsubsection 2.1.2), this interpolation process cannot reflect exactly the real ray geometry. For both cases, $\Delta\Phi_{\mathrm{aramis}}$ and the PRO observation agree best at lower altitudes, except for the lower peak in panel (b). This closer agreement at low altitudes is consistent with the findings of Paz et al. (2024), who similarly reported better consistency between PRO and US NEXRAD radar-derived $\Delta\Phi$ below the melting layer.

https://doi.org/10.5194/egusphere-2026-4040
Preprint. Discussion started: 16 July 2026

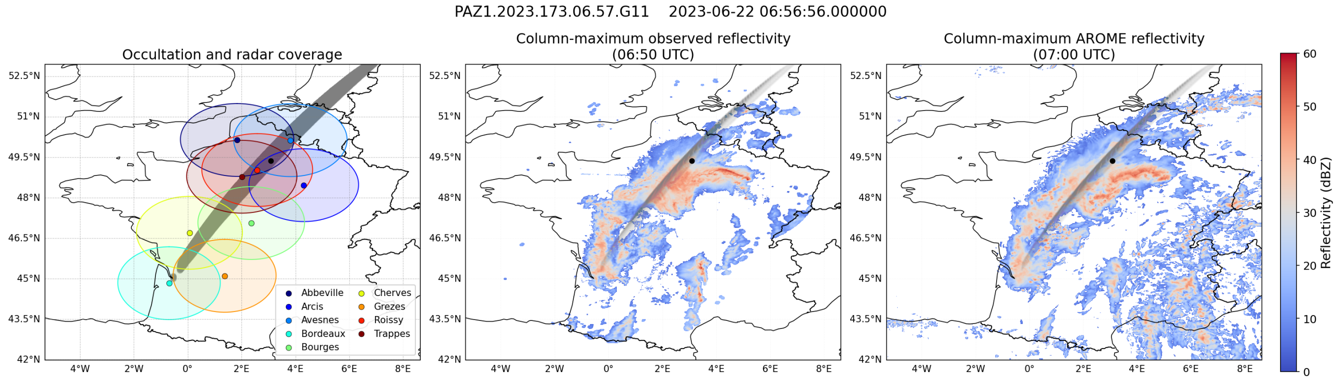

Figure 2. Combined view of the radio-occultation geometry, the co-located observed radar reflectivity, and the AROME-simulated reflectivity for case PAZ1.2023.173.06.57.G11. **Left:** PRO ray trajectories below 20 km altitude (grey points) and the occultation point (black dot), shown together with the Météo-France weather radars whose 150 km coverage circles intersect the occultation footprint (coloured circles and markers, one colour per radar). **Middle:** column-maximum reflectivity (dBZ) from the ARAMIS three-dimensional composite at 06:50 UTC, the closest acquisition time to the occultation. **Right:** column-maximum reflectivity (dBZ) simulated by AROME at 06:00 UTC, the closest forecast valid time. The PRO ray trajectory is overlaid in grey on the two reflectivity panels, shown with higher transparency than in the left panel to preserve visibility of the underlying reflectivity field. The same dBZ colour scale is used in both reflectivity panels to facilitate direct comparison.

In panel (a), $\Delta\Phi_{\mathrm{aramis}}$ also shows a pronounced negative peak between approximately 10 and 12 km, where the PRO observation is positive. After applying a more restrictive quality control filter, removing the K_{dp} values associated with a $\rho_{\mathrm{HV}} < 0.9$, the negative signature in the $\Delta\Phi_{\mathrm{aramis}}$ data persists. This indicates that it is unlikely to be due to low-quality returns due to nonuniform beam filling NBF (see for example section 6.8 of Ryzhkov and Zrnić, 2019, for a detailed explanation of NBF). We interpret this peak as the signature of vertically-oriented pristine ice crystals in the upper troposphere: when ice particles are aligned with their major axis along the vertical rather than the horizontal, the sign of K_{dp} reverses and the locally derived $\Delta\Phi$ takes negative values. The PRO observation does not display the same negative signature, which we attribute to two effects. First, a sampling mismatch between the two geometries: each ARAMIS radar scans the atmosphere at only eight discrete elevation angles, so the radar volumes intersected along the PRO ray path are sparse, whereas the PRO observation provides a continuous integration along the entire ray. Second, at $\sim$7.5 km and above, the radar volumes intersected by the PRO ray path are increasingly far from the corresponding radar sites and the number of overlapping volumes at those altitudes is reduced, so the radar-derived $\Delta\Phi$ may be dominated by a small number of pixels that are not representative of the full column sampled by the PRO ray.

Although the comparison is limited to two well-covered cases, the available evidence suggests that the agreement between $\Delta\Phi_{\mathrm{aramis}}$ and the PRO observation is closest below the melting layer, while above it the two measurements diverge, with $\Delta\Phi_{\mathrm{aramis}}$ taking systematically smaller values than the PRO observation. This divergence at higher altitudes is consistent with Paz et al. (2024), who similarly found weaker agreement between PRO and radar-derived observations at higher altitudes.

https://doi.org/10.5194/egusphere-2026-4040
Preprint. Discussion started: 16 July 2026

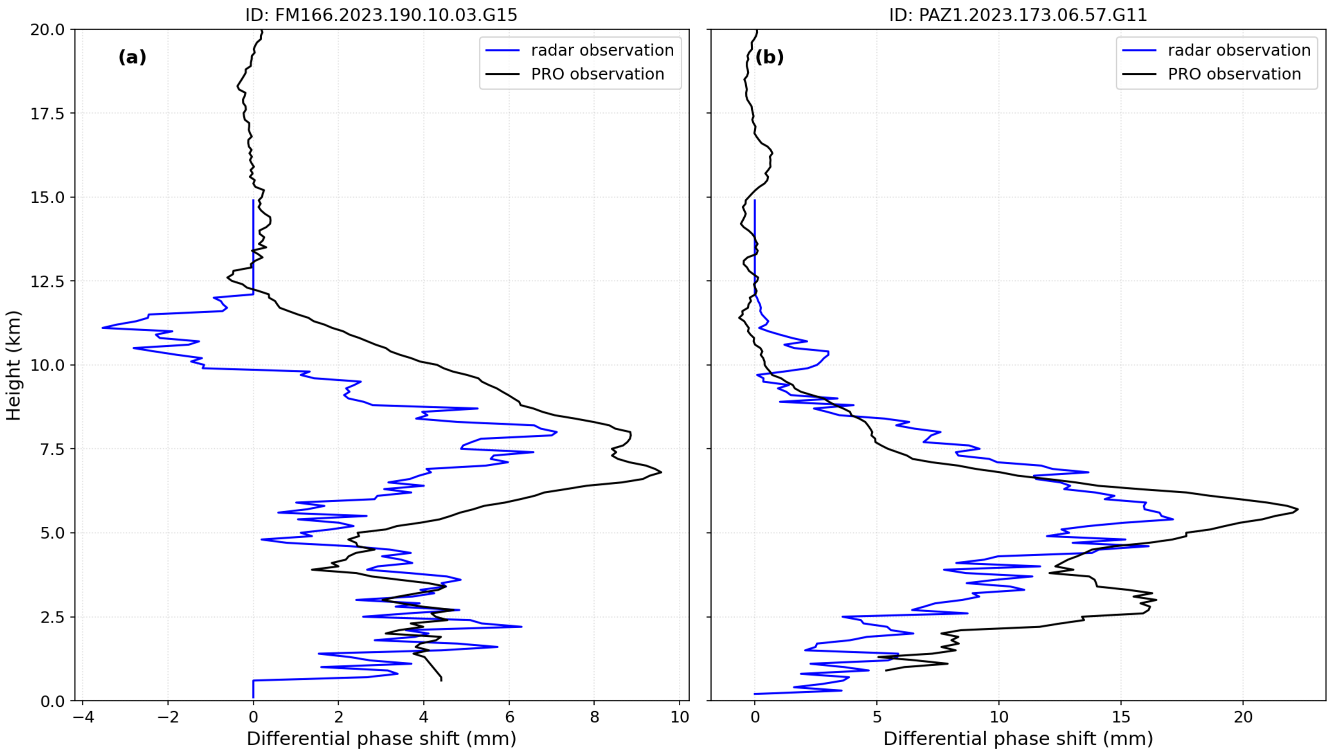

Figure 3. $\Delta\Phi_{\mathrm{aramis}}$ for cases FM166.2023.190.10.03.G15 (a) and PAZ1.2023.173.06.57.G11 (b) obtained by integrating along the PRO ray path the K_{dp} measured by the ARAMIS radar network.

285 Strictly speaking, neither measurement constitutes an absolute reference, so this difference cannot be unambiguously attributed to an underestimation by either of them.

3.2 Operator comparison

We now turn to a quantitative comparison of the two operators across the full sample of occultations, using the PRO operator with the merged graupel configuration (explained and justified in Section 3.3) and the scattering efficiencies retrieved from the global Bayesian inversion, i.e., the single set of parameters obtained by jointly inverting all 27 occultations rather than region-specific retrievals.

Figure 4 shows the height-resolved median difference between observed and simulated $\Delta\Phi$ for the PRO operator (red) and operadar (blue), for the whole sample (top-left panel) and per geographical domain. The first observation drawn from this comparison is that both operators broadly reproduce the observed $\Delta\Phi$ across the full tropospheric column: the median differences remain within a few millimetres at all altitudes and in all regions, indicating that both forward operators capture the leading-order vertical structure of the polarimetric signal produced by frozen and liquid hydrometeors in AROME and AROME-OM. Within this overall agreement, however, two systematic discrepancies emerge.

https://doi.org/10.5194/egusphere-2026-4040
Preprint. Discussion started: 16 July 2026

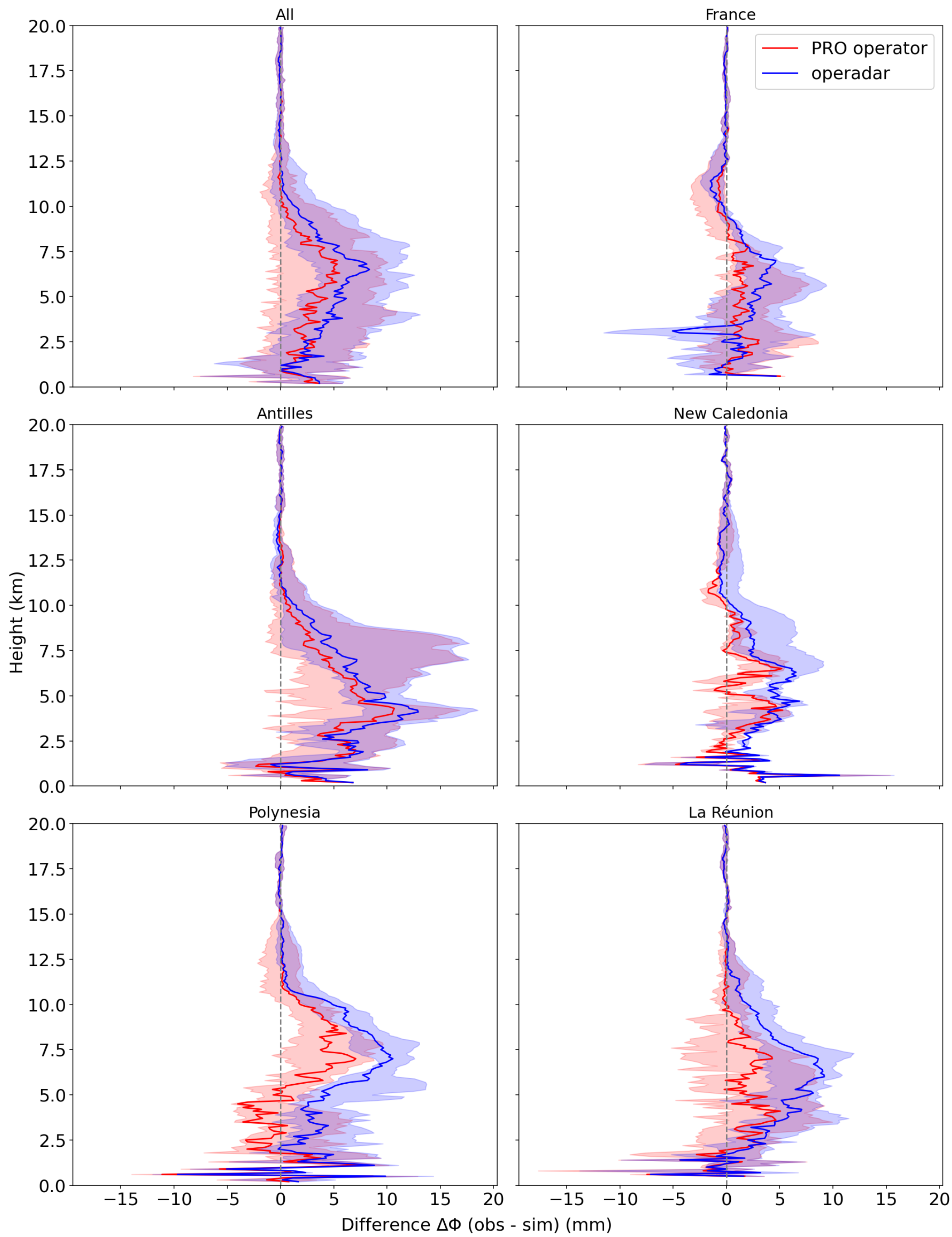

Figure 4. Height-resolved median $\Delta\Phi$ bias (observation minus simulation) for the PRO operator (red) and operadar (blue). Shading shows the 16th-84th percentile range. First panel left shows the bias for all cases analyzed, while the rest of the panels illustrate this bias for the different geographical regions. The scattering efficiencies used in the PRO operator were those obtained from the global optimization (i.e. considering all the sample cases).

https://doi.org/10.5194/egusphere-2026-4040
Preprint. Discussion started: 16 July 2026

The first is shared by both operators: the median differences are positive across most of the tropospheric column in every region, meaning that both operators yield smaller $\Delta\Phi$ values than observed. Moreover, the two profiles tend to share a similar vertical shape, with their respective discrepancies growing and decaying together as a function of altitude in most regions, even where their absolute magnitudes differ. This co-variation indicates that the two operators are responding to the same underlying feature of the model fields rather than developing independent biases. Because $\Delta\Phi$ is most sensitive to the path-integrated frozen content, this shared discrepancy is most plausibly attributed to an underestimation of frozen hydrometeors, snow and graupel in particular, as identified in Sec. 3.3, in the underlying AROME and AROME-OM forecasts, and is most pronounced over the four tropical regions where convective frozen content is most affected by parameterization uncertainties.

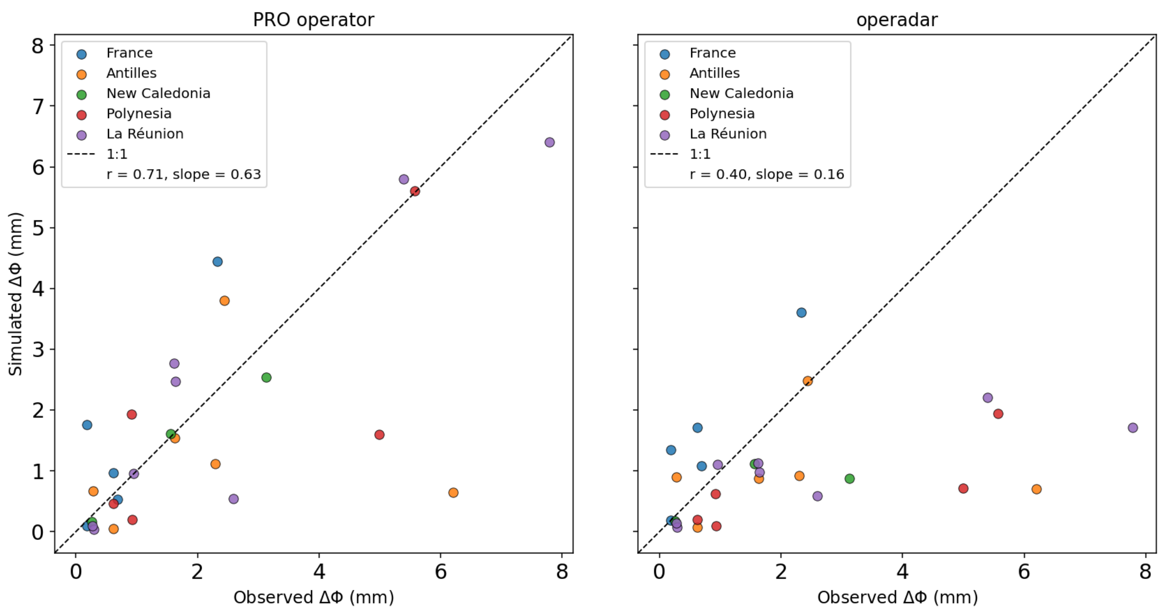

Figure 5. Scatter plot showing the relation between observed and simulated $\Delta\Phi$, for PRO operator (left) and operadar (right). Each point represents an occultation, specifically the median of the $\Delta\Phi$ profile.

The second is specific to operadar and accounts for the residual difference between the two operators: while the PRO operator achieves a smaller absolute discrepancy than operadar at practically every altitude, the operadar difference is characterized by a more pronounced positive offset throughout the mid and upper troposphere, attributable to its low sensitivity to snow, and a further deviation below ∼3 km driven by the bright-band and wet-graupel contributions. The PRO operator reduces both of these systematic features, demonstrating that the use of optimized parameters yields a more realistic representation of $\Delta\Phi$. Nonetheless, the fact that operadar still captures the leading-order vertical structure of the PRO operator results across the four tropical regions, where it has never previously been evaluated, is itself a noteworthy result, and indicates that its development context over metropolitan France generalizes reasonably well to tropical convective regimes. Despite the small number of cases

https://doi.org/10.5194/egusphere-2026-4040
Preprint. Discussion started: 16 July 2026

per region, the agreement over France outperforms that over the more convective tropical regions, suggesting that the more stratiform mid-latitude environment is better represented by the forecasts and the operators alike.

The pooled relationship between observed and simulated $\Delta\Phi$ is shown in Fig 5. Each marker represents one occultation, summarized as the median of the $\Delta\Phi$ profile, with each colour associated with a different region. The PRO operator yields a substantially better correlation with the observations (r = 0.70, slope = 0.61) than operadar (r = 0.31, slope = 0.14). The points follow more closely the 1:1 line for the PRO operator, particularly in the moderate $\Delta\Phi$ region. For larger values of $\Delta\Phi$ it is not that clear, both operators struggle to better represent those cases with higher values of $\Delta\Phi$. However, this is more noted for operadar, that systematically underestimates $\Delta\Phi$, specially for those observations exceeding a median $\Delta\Phi$ of $\sim$3-4 mm. The operadar underestimation is most notable over the four tropical regions, where the markers cluster well below the 1:1 line, while the French points sit closest to it. This is consistent with the fact that operadar has been developed and tuned primarily against ARAMIS observations over metropolitan France (Augros et al., 2016; David et al., 2025), in mid-latitude conditions, and has not previously been evaluated against tropical convective events. The PRO operator, by contrast, is calibrated against the pooled observations from all 27 occultations through the global Bayesian inversion, rather than being tuned to a single mid-latitude regime, which translates into a more uniform behaviour of the scatter across regions. However, in this kind of more convective environments a temperature-dependent implementation of the PRO operator could be interested to test, as in Paz et al. (2026), but this is out of the scope of this study.

Table 1. Summary metrics for the PRO and operadar operators, computed over the pooled sample (*All*) and per region. RMSE and Bias are in mm; χ^2_ν is the reduced chi-squared based on the PRO observation uncertainty.

Region	Operator	RMSE (mm)	Bias (mm)	χ^2_ν
All	PRO	4.266	1.559	1.572
	operadar	5.165	2.535	2.423
France	PRO	2.982	0.494	0.979
	operadar	3.494	0.694	1.063
Antilles	PRO	5.919	2.697	3.236
	operadar	6.643	3.568	4.098
Polynesia	PRO	3.994	1.081	1.357
	operadar	5.585	3.302	3.480
New Caledonia	PRO	2.250	0.451	0.208
	operadar	3.441	1.765	0.686
La Réunion	PRO	3.450	0.748	0.707
	operadar	4.984	2.691	1.943

https://doi.org/10.5194/egusphere-2026-4040
Preprint. Discussion started: 16 July 2026

Summary metrics are given in Table 1. Across the whole sample, the PRO operator reduces the RMSE from 5.17 mm to 4.27 mm, the bias from 2.54 mm to 1.56 mm, and the reduced chi-squared from 2.42 to 1.57 relative to operadar. The improvement is systematic across every region. For the PRO operator the reduced chi-squared approaches unity in several regions, indicating that the global retrieval brings the operator into approximate consistency with the nominal PRO observation uncertainties, whereas operadar retains $\chi^2_\nu > 2$ in most of the regions.

Taken together, these results are consistent with what could reasonably be expected from the comparison: under the conditions sampled here, the PRO operator achieves closer agreement with the PRO observations than operadar does, both in the height-resolved bias structure and in the per-occultation correlation, with the largest differences between the two operators arising over the tropical convective regions where operadar has not previously been evaluated. The results should therefore be interpreted not as a benchmark of absolute operator quality but as a measurement of how each operator, taken on its own terms, responds to the PRO observations and the underlying AROME and AROME-OM fields across regimes ranging from mid-latitude convective and stratiform to tropical convective.

3.3 Hydrometeor contributions to $\Delta\Phi$

Having shown that the simulated $\Delta\Phi$ profiles produced by the two operators differ systematically, we now examine the physical origin of these discrepancies by decomposing the $\Delta\Phi$ difference between the two operators by hydrometeor species, namely cloud water, rain, pristine ice, snow, and graupel (further split into dry and wet graupel, as diagnosed by operadar; see Sect. 2.4). It is worth emphasizing that the goal of this section is to identify the species and altitude ranges that drive the differences, rather than to establish that one operator performs better than the other: such a judgment would require a reference observation that is independent of both operators. Moreover, the PRO operator parameters have been optimized against the same 27 cases under consideration, while operadar has not been retuned for this dataset. Figure 6 shows the height-resolved median $\Delta\Phi$ difference between PRO operator and operadar decomposed by species across the full observation sample. Positive values indicate that the PRO operator attributes more $\Delta\Phi$ to a given species than operadar does at that altitude range.

The snow contribution is consistently positive and extends from the melting layer up to higher levels, confirming that the contrasting treatment of snow is the principal driver of the systematic difference between the two operators. The underestimation of the $\Delta\Phi$ signal in snow with operadar (as compared to the PRO operator) is not surprising and confirms a difficulty to simulate a positive K_{dp} signal in snow using T-matrix scattering simulations while keeping consistent with the model mass-size relationship and PSD as underlined in David et al. (2025) and also shown in the improved version of operadar proposed by David (2026).

Several studies employing polarimetric radar forward operators to evaluate model simulations have highlighted a systematic underestimation of the specific differential phase K_{dp} in snow regions. Köcher et al. (2022) and Shrestha et al. (2022) observed this underestimation across different microphysics schemes and radar forward operator parameterizations. In a stratiform event, Shrestha et al. (2022) demonstrated that snow dominated above the melting layer. Despite testing a variety of snow shapes and orientations, their simulations failed to reproduce the observed polarimetric values at these altitudes. This persistent underestimation of dual-polarization variables in snow may stem from the overly simplistic representation of snow aggregates

https://doi.org/10.5194/egusphere-2026-4040
Preprint. Discussion started: 16 July 2026

as homogeneous spheroids using the T-matrix method, a limitation also noted by Trömel et al. (2023) and supported by the findings of Schrom and Kumjian (2018).

The PRO operator, in turn, obtains its snow scattering efficiency from the observations through Bayesian inversion, and that inversion consistently demands a much larger snow signal to reproduce the observed $\Delta\Phi$. Within its own framework, the PRO operator therefore identifies snow as the dominant contributor at practically every altitude above the melting layer, consistent with the snow-dominated picture obtained in the WRF and IFS analyses of Paz et al. (2025, 2026).

The wet-graupel contribution, by contrast, is strongly negative in a narrow layer between ∼2.5 and ∼5 km in essentially every region, indicating that operadar attributes substantially more $\Delta\Phi$ to the bright-band wet graupel than the PRO operator does. This signature reflects operadar's bright-band parameterization, which diagnoses a fraction of dry graupel as melting and assigns it a high effective dielectric constant, producing a localized K_{dp} enhancement that the PRO operator does not reproduce. In the PRO forward operator framework, this feature is only weakly constrained by the observations: the Bayesian inversion attempts to reproduce the small low-level signal by inflating x_{wg} to unphysically large values, and when applied globally the inflated efficiency then produces a systematic overestimation of $\Delta\Phi$ near the melting layer. The ice contribution is also negative at upper levels, where the PRO operator has lower sensitivity than operadar, which could be mainly due to the very low axis ratio (0.2) assumed for pristine ice in the new operadar configuration (David, 2026). The graupel difference is generally the smallest of the four species and is concentrated around the melting layer, with the exception of New Caledonia.

It is worth clarifying at this point that the graupel and wet-graupel contributions shown in Fig. 6 correspond to a version of the PRO operator that retains the separate treatment of the two categories, so as to make them directly comparable, species-by-species, with the corresponding operadar output. The wet-graupel category is, however, weakly constrained by the PRO observations: it is confined to a narrow layer around the melting level and typically accounts for only a small fraction of the total path-integrated frozen water content, so its along-ray contribution to $\Delta\Phi$ is small relative to that of snow and pristine ice, which extend over a much deeper layer of the troposphere. As a result, the Bayesian inversion has little information from which to constrain x_{wg} independently, and small residuals near the melting layer can drive the retrieved efficiency to disproportionately large values in order to compensate. Given this weak observational constraint on the wet-graupel category, we adopt in previous and all subsequent sections, both the operator-comparison metrics of Sec. 3.2 and the scattering-efficiency retrievals of Sec. 4, a merged graupel configuration of the PRO operator, in which dry and wet graupel are combined into a single species $x_{\mathrm{gg+wg}}$ consistent with the single prognostic graupel variable of AROME. Where the term "graupel" appears in subsequent sections without further qualification, it should therefore be understood as this merged category.

4 Evaluation of global and km-scale NWP models using PRO

The preceding section used the PRO observations to intercompare two forward operators driven by the same model fields. We now use the PRO forward operator, with the merged graupel configuration, to analyze the scattering efficiency output across AROME/AROME-OM and ARPEGE. Under this framing, the scattering efficiency parameters become a diagnostic tool of how each model distributes the frozen water content among its prognostic species, rather than a property of the operator itself.

https://doi.org/10.5194/egusphere-2026-4040
Preprint. Discussion started: 16 July 2026

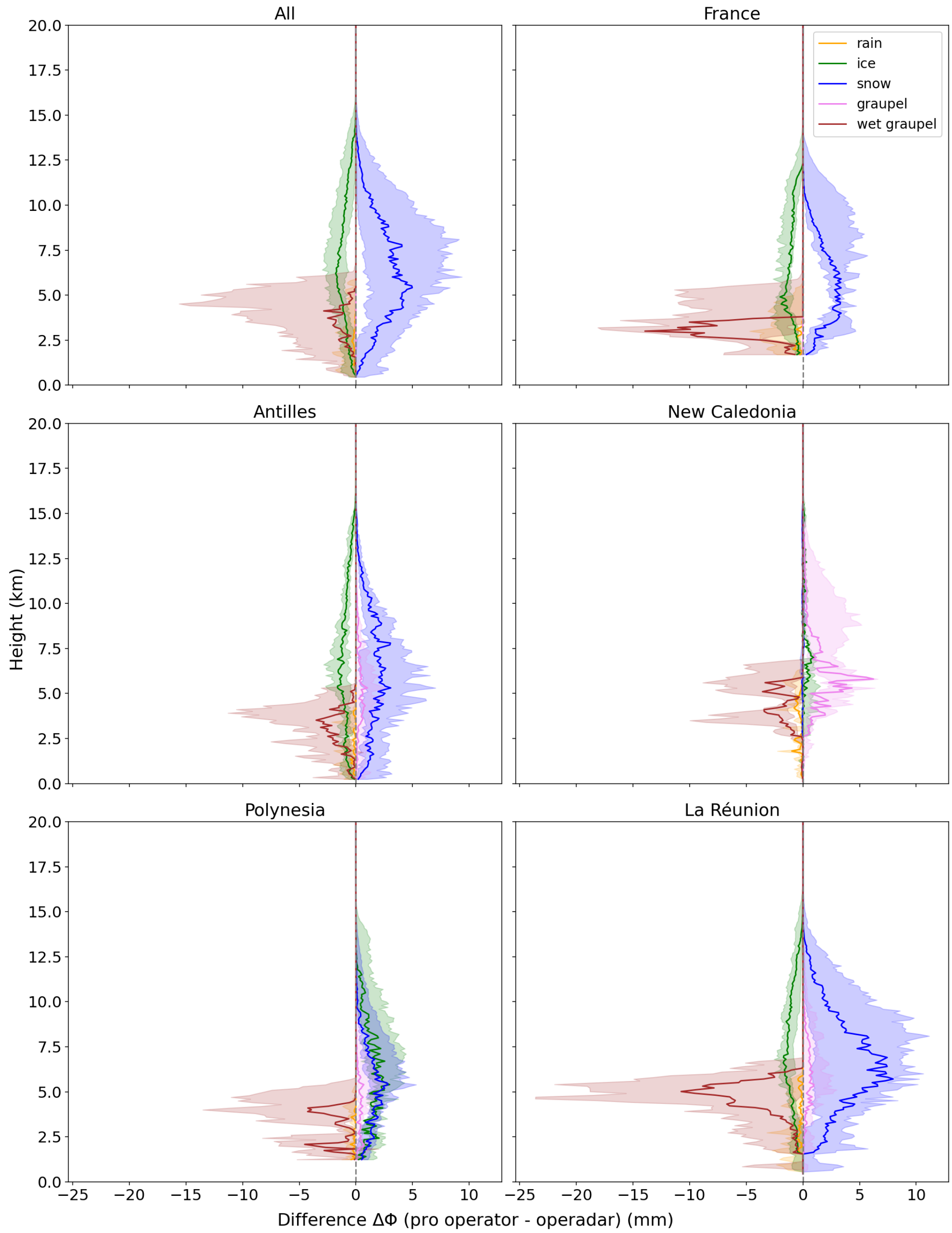

Figure 6. Height-resolved median difference in $\Delta\Phi$ between the PRO operator and operadar, decomposed by hydrometeor species. The top-left panel shows the difference for all cases; the remaining panels show the difference for each of the geographical regions considered.

https://doi.org/10.5194/egusphere-2026-4040
Preprint. Discussion started: 16 July 2026

4.1 Evaluation of ARPEGE/AROME/AROME-OM

Table 2 reports the globally and regionally retrieved parameter efficiencies for the two model configurations: one driven by ICE3 microphysics of AROME and AROME-OM; and one driven by Lopez (2002) in ARPEGE. These two configurations apart from being a regional vs global NWP model, differ on the frozen hydrometeor distributions. While AROME considers snow, ice and graupel, ARPEGE considers stratiform snow, ice and convective snow. Larger values of x_i would correspond to highly aspheric, horizontally aligned particles (plates, dendrites or large snow aggregates), that produce a strong scattering. Whereas small values of x_i correspond to more spheroidal habits, particles with weaker preferential orientation, or smaller crystals.

Table 2. Retrieved scattering efficiency parameters (mm (kg m^{-2})$^{-1}$) for the PRO operator driven by AROME (metropolitan France) and AROME-OM (overseas territories), and by the ARPEGE global model. x_{graupel} denotes the merged dry+wet graupel species in AROME; ARPEGE distinguishes stratiform (x_{snow}) and convective (x_{csnow}) snow and carries no explicit graupel category.

Model	Parameter	Global	France	Antilles	Polynesia	New Cal.	Reunion
AROME	x_{snow}	0.195	0.138	0.141	0.088	0.009	0.216
	x_{ice}	0.001	0.040	0.001	0.750	0.303	0.037
	x_{graupel}	0.001	0.001	0.054	0.080	0.290	0.064
ARPEGE	x_{snow}	0.054	0.106	0.048	0.081	0.058	0.010
	x_{ice}	0.088	0.033	0.076	0.079	0.140	0.134
	x_{csnow}	0.030	0.057	0.046	0.052	0.060	0.014

Figure 7 complements Table 2 by displaying the same retrieved scattering efficiencies graphically, allowing a direct visual evaluation of the relative magnitude and regional variability of each hydrometeor's contribution within the two models.

The AROME retrieval displays a strongly regime-dependent pattern. In France, the Antilles and globally, snow is the only species making a finite contribution, with x_{ice} and x_{graupel} collapsing to the prescribed lower bound of optimization (10^{-3} mm (kg m^{-2})$^{-1}$), while the retrieved x_{snow} takes moderate values consistent with horizontally-oriented aspheric particles. Over Polynesia and New Caledonia the qualitative picture changes: x_{ice} reaches the largest values of the dataset (0.750 and 0.303 respectively), x_{graupel} becomes the most effective contributor over New Caledonia (0.290), and x_{snow} itself collapses to the lower bound. Regionally, every AROME parameter therefore spans nearly its full retrieval range across the five domains, with individual species alternating between the saturated lower bound and the most effective contribution. This large regional spread indicates that the retrieved AROME parameters are highly sensitive to the specific meteorological situation of each region, and, given the small number of cases per region (three to eight), does not support quantitative conclusions being drawn from the individual regional retrievals. We therefore adopt the global AROME retrieval as the operationally usable parameter set and read the per-region values as indicative rather than definitive.

https://doi.org/10.5194/egusphere-2026-4040
Preprint. Discussion started: 16 July 2026

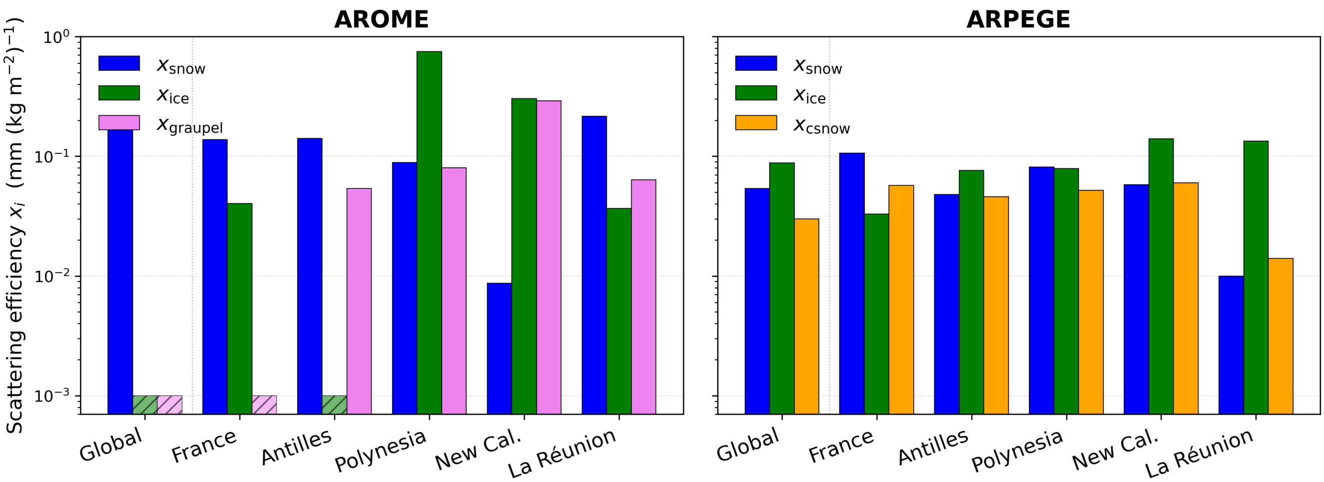

Figure 7. Retrieved scattering efficiency parameters x_i (mm (kg m^{-2})$^{-1}$) for the PRO operator driven by AROME/AROME-OM (left) and ARPEGE (right), shown on a logarithmic scale for the global retrieval and each of the five geographical regions. For AROME, hatched bars denote parameters that collapse to the prescribed lower bound of the optimization (10^{-3} mm (kg m^{-2})$^{-1}$), indicating that the corresponding species is not required by the inversion to reproduce the observed $\Delta\Phi$ in that region. ARPEGE distinguishes stratiform snow (x_{snow}) and convective snow (x_{csnow}) and carries no explicit graupel category.

The ARPEGE retrieval displays a strikingly different behavior. None of the ARPEGE parameters saturate at the lower bound: stratiform snow, ice and convective snow each make a non-negligible contribution in every region, and the regional variability of the parameters is much weaker than that of AROME, with no region exhibiting the single-species dominance seen in the AROME retrievals. This comparatively flat behavior is consistent with a model that spreads the frozen-column mass more evenly across its prognostic species than AROME. It is worth emphasizing, however, that the AROME and ARPEGE retrievals are not directly comparable at the value level of x_i: the two models differ in grid, physics and microphysics, and the effective scattering efficiency retrieved by the operator absorbs all of these differences together with the underlying scattering properties of the frozen particles. The retrievals should therefore be read as two independent characterizations of how each model, on its own terms, translates its microphysical fields into the observed $\Delta\Phi$.

A methodological aspect that is likely relevant to the different retrieved patterns between the two models is the treatment of the precipitation fraction. In ARPEGE, convective snow and rain are conventionally assumed to occupy about 5% of the horizontal grid cell, whereas in AROME the graupel species typically covers the full $1.3\,\mathrm{km} \times 1.3\,\mathrm{km}$ grid. Passing the raw hydrometeor contents to the PRO forward operator without correcting for the model-resolved precipitation fraction, as done here, is therefore consistent between the two models only in a formal sense. In the microwave forward operators used operationally to simulate passive and active satellite observations in global NWP systems, hydrometeor contents are normalized by the precipitation fraction before being passed to the operator (Geer et al., 2021; Mangla et al., 2025), and the same normal-

https://doi.org/10.5194/egusphere-2026-4040
Preprint. Discussion started: 16 July 2026

ization would be expected to affect the ARPEGE retrievals more strongly than the AROME ones. The sensitivity of the PRO forward operator to the precipitation fraction is left for a future study.

5 Discussion

The results presented in the two previous sections show that PRO observations carry information at two distinct levels. They discriminate between forward operators that map the same model fields into $\Delta\Phi$ (Section 3.2), and they discriminate between NWP models when read through a common forward operator (Section 4). The following discussion takes these two analyses and synthesizes their joint implications for the use of PRO in NWP.

The most relevant result of the operator comparison is the difference in the snow contribution between the two operators. In operadar, snowflakes are assigned a low density (consistently with the AROME ICE3 microphysics scheme), and a probably too simplistic representation as oblate spheroids, which limits their K_{dp} signature; in the PRO operator, the linear relation between K_{dp} and WC is calibrated against the observations, and the inversion consistently demands a relatively large snow efficiency to reproduce the observed $\Delta\Phi$. In addition, because $\Delta\Phi$ is the integral of K_{dp} along the entire ray path and snow typically occupies a deep layer of the troposphere, even a moderate per-unit-mass efficiency accumulates into a large path-integrated signal. This interpretation is reinforced by the cross-check against the ARAMIS ground-based polarimetric radar network (Sec. 3.1): the radar-derived $\Delta\Phi_{\mathrm{aramis}}$, constructed from observations alone, also undershoots the PRO observation around the peak altitudes. In that case the radar underestimation could arise in part from the undersampling of the snow region by the ARAMIS network, as the radar beams gets larger at higher altitudes which can dilute the K_{dp} values.

The per-species decomposition of the operator difference also revealed wet graupel as the principal negative contributor near the melting layer (Figure 6), a direct manifestation of operadar's bright-band parameterization. As discussed in Sec. 3.3, the wet-graupel signature is confined to a narrow layer and typically accounts for only a small fraction of the total path-integrated frozen content, particularly in more convective cases where this layer is thinner or less well sampled. This makes x_{wg} weakly constrained whenever the wet-graupel water content is small relative to the total frozen column, and the inversion is then liable to inflate it. The merged graupel formulation removes this degree of freedom and improves consistency with observations, illustrating that this feature has a higher level of microphysical detail than can be well constrained by this configuration of the PRO operator. However, a similar approach as in Paz et al. (2026) with a temperature-dependent scattering efficiency could be a valuable next step in this direction.

Although the PRO operator achieves closer agreement with the observations than operadar, the two are best viewed as complementary. Operadar provides spatially and temporally dense polarimetric fields and resolves the melting layer in detail, while PRO offers all-weather, and strong sensitivity to the frozen part of the column, particularly snow. The fact that both operators can be used under the same model fields enables their joint use to cross-validation of microphysical parameterizations.

Turning to the model comparison, the retrieved scattering efficiencies provide a fingerprint of how each NWP model distributes the frozen water content among its prognostic species, with each retrieval understood on its own terms. Figure 8 substantiates this reading directly at both the column-integrated and vertical-profile levels. Panel (f) shows the total frozen in-

https://doi.org/10.5194/egusphere-2026-4040
Preprint. Discussion started: 16 July 2026

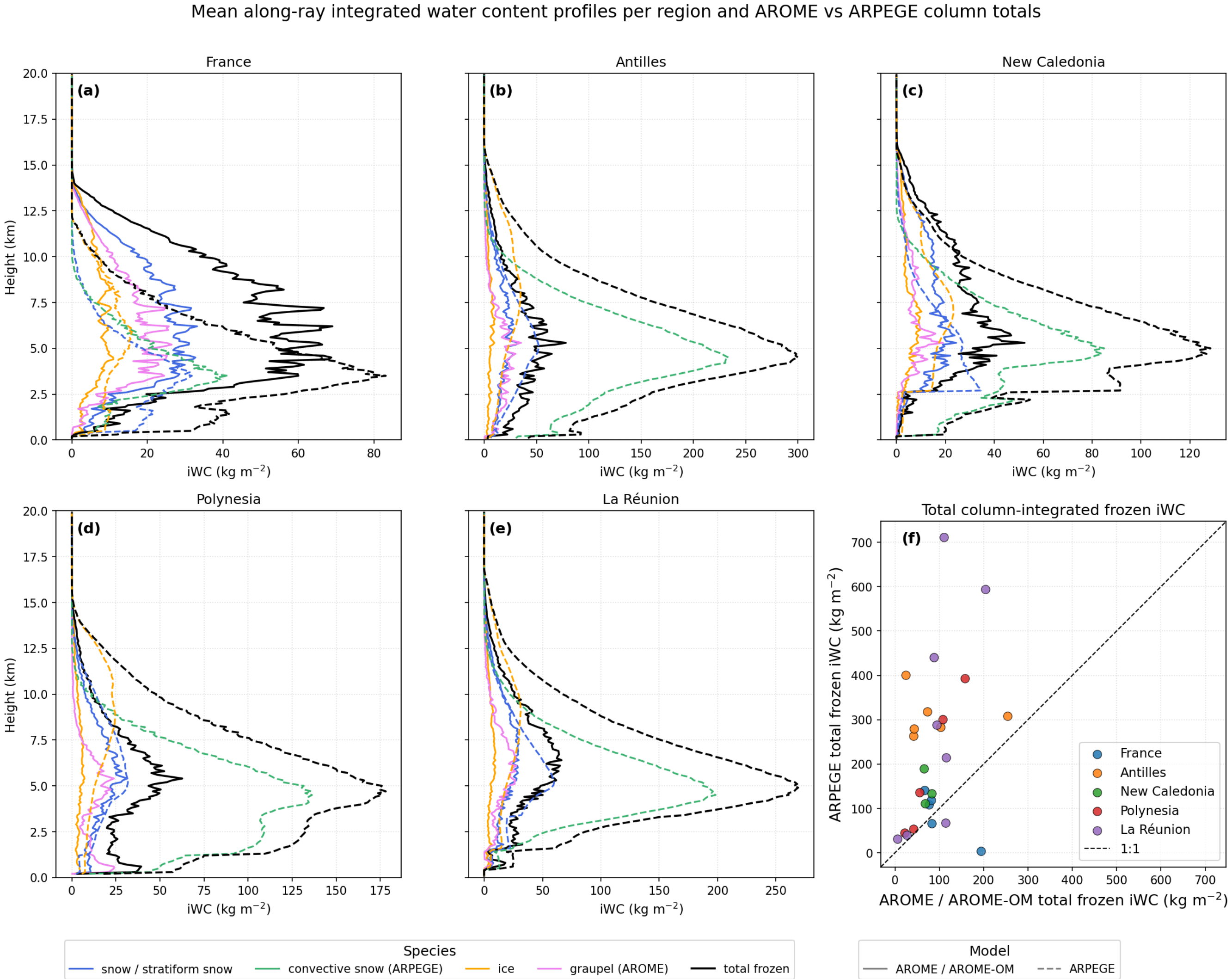

Figure 8. Combined view of the mean along-ray integrated frozen water content (iWC) per region (panels a-e) and the corresponding column totals (panel f). **(a-e)** Mean along-ray integrated water content profiles for each of the five regions, comparing AROME / AROME-OM (solid lines) and ARPEGE (dashed lines). Coloured lines show each frozen species: snow / stratiform snow (blue), convective snow (green, ARPEGE only), ice (orange) and graupel (magenta, AROME only); the black line is the total frozen water content. Each profile is the regional mean over the cases listed in Table A1. **(f)** Total column-integrated frozen iWC from ARPEGE plotted against that from AROME / AROME-OM for each of the 27 occultations; colour denotes the geographical region, the dashed line is the 1:1 reference. The systematic offset of points above the 1:1 line indicates that ARPEGE produces a larger frozen-column mass than AROME, with the largest excesses occurring over the tropical regions.

tegrated WC (iWC) for each of the 27 occultations: the points are systematically distributed above the 1:1 line, indicating that

https://doi.org/10.5194/egusphere-2026-4040
Preprint. Discussion started: 16 July 2026

ARPEGE produces more frozen mass than AROME in nearly every case, with the largest excess occurring over the tropical regions. Panels (a-e) show the same comparison resolved vertically and by species. Over metropolitan France, AROME and ARPEGE produce comparable total amounts, although the vertical distribution differs: AROME spreads mass between snow and graupel through the mid and upper troposphere, while ARPEGE concentrates a substantial fraction in a lower-tropospheric peak associated with convective snow. The comparatively better agreement between the two models over Western Europe is likely aided by the smaller horizontal grid spacing of ARPEGE over this domain (∼5,km) and by the associated cloud and precipitation fraction, which are closer to the AROME configuration than they are over the overseas territories. Over the four tropical regions the contrast is far more pronounced: the ARPEGE total frozen profile exceeds the AROME total by factors of three to seven near 5,km. The decomposition shows that the convective snow species in ARPEGE, which has no direct counterpart in AROME, accounts for almost all of this additional mass, and the inversion associates it with a small scattering efficiency, consistent with the ARPEGE convective-snow parameter reported in Sec. 4. As noted in Sec. 4, ARPEGE's convective snow is conventionally assumed to occupy only about 5% of the horizontal grid cell, whereas the corresponding AROME graupel typically covers the full $1.3\,\mathrm{km} \times 1.3\,\mathrm{km}$ grid; since the hydrometeor contents are passed to the PRO operator without correcting for this precipitation fraction, part of the large excess frozen mass attributed to ARPEGE in the tropics is likely an artifact of this grid-scale mismatch rather than a genuine difference in simulated frozen water content.

6 Conclusions and perspectives

This study has presented the first evaluation of a hydrometeor-specific PRO forward operator using the AROME and AROME-OM convection-permitting models and the global NWP model ARPEGE, together with a systematic intercomparison against the operadar polarimetric radar forward operator. Drawing on 27 PRO occultations spanning metropolitan France and four overseas territories, the work has exercised two complementary intercomparisons: an operator-level comparison (PRO versus operadar, both driven by the same AROME / AROME-OM hydrometeor fields), and a model-level evaluation (AROME / AROME-OM versus ARPEGE, both read through the PRO operator).

At the operator level, the PRO operator achieves closer agreement with the observations than operadar across all five regions, reducing the RMSE, the bias, and the reduced chi-squared over the whole sample. The improvement is systematic at every altitude and, through the per-species decomposition of the operator difference, traced primarily to the contrasting treatment of snow: the PRO operator identifies snow as the dominant contributor at practically all altitudes above the melting layer, whereas operadar attributes most of the signal to wet graupel through its bright-band parameterization. The merged graupel formulation introduced here, which combines dry and wet graupel into a single prognostic species as the partition that AROME does, removes a poorly constrained degree of freedom near the melting layer and produces $\Delta\Phi$ profiles substantially closer to the observations. A cross-check against $\Delta\Phi_{\mathrm{aramis}}$ derived from ground-based polarimetric radar over metropolitan France provides an independent observational anchor for the PRO operator results.

At the model level, the retrieved scattering efficiencies act as a diagnostic of how each NWP model distributes the frozen water content among its prognostic species. The AROME and AROME-OM forecasts produce a pronounced regional finger-

https://doi.org/10.5194/egusphere-2026-4040
Preprint. Discussion started: 16 July 2026

print, snow-dominated over France and the Antilles, with more ice and graupel in the deep convection of Polynesia and New Caledonia, also with several efficiencies collapsing to the prescribed lower bound. The global ARPEGE model, by contrast, produces systematically smaller and more uniformly distributed parameters that remain in the interior of their prior range, consistent with a more even spread of the frozen-column mass over snow, ice and convective snow and with the absence of an explicit graupel category.

The hydrometeor-specific PRO operator was introduced and characterized in two preceding studies that are complementary to the present one. Paz et al. (2025) applied the formulation to a single NWP model, the Weather Research and Forecasting (WRF) system, and used it to discriminate between different microphysics scheme configurations within that model in Atmospheric River (AR) conditions, demonstrating that PRO observations carry sufficient information to constrain frozen-particle habit assumptions. Paz et al. (2026) developed an operational version of the operator at ECMWF, evaluated it against the offline Hotta et al. (2024) baseline on 23 AR cases, and introduced a temperature-dependent snow scaling parameter that further improved agreement with the observations. The present article moves the focus from single-model evaluation to multi-model intercomparison: the PRO operator is held fixed and used as a diagnostic of two operational Météo-France systems with markedly different microphysics (ICE3 in AROME and Lopez (2002) in ARPEGE), and confronted with an entirely different operator, the polarimetric radar operator operadar, driven by the same model fields. The geographical sample is also extended including tropical convective regimes over the Météo-France overseas territories, and the analysis is anchored by an independent observational reference: ground-based polarimetric radar over metropolitan France. Whereas the WRF analysis kept the host model fixed and varied the microphysics, and the IFS analysis kept the host model fixed and varied the operator, the present study varies both axes simultaneously, exercising the dual role of PRO as both operator-discriminator and model-discriminator. Together with analyses from Paz et al. (2025, 2026), this work establishes the hydrometeor-specific PRO operator as a versatile diagnostic that can be used across NWP systems of different complexity, resolution and microphysical formulations, and confirms that PRO observations are operationally robust as a constraint on frozen-hydrometeor microphysics, and also could serve as a diagnostic of other types of operator, specifically radar operators.

A natural next step is the temperature dependent extension of the operator, specially across the AROME-OM observations, the construction of a substantially larger co-location database that better samples the regime diversity, and the testing of the PRO operator within a data assimilation framework in order to quantify the impact of PRO observations on the analyzed frozen-hydrometeor fields.

Appendix A: List of PRO occultations

The 27 PRO occultations analyzed in this study, listed in Table A1, were drawn from PAZ and Spire acquisitions between March 2023 and January 2025, and were selected on the basis of a substantial differential phase shift signal co-located in space and time with available AROME, AROME-OM and ARPEGE simulations. The cases are grouped into the five geographical regions covered by the Météo-France operational suite, metropolitan France (5 cases), the Antilles (6), La Réunion (8), French

https://doi.org/10.5194/egusphere-2026-4040
Preprint. Discussion started: 16 July 2026

Polynesia (5) and New Caledonia (3), and together span both mid-latitude stratiform regimes and tropical convective regimes. Each occultation is identified by its *roid*.

Table A1: The 27 PRO occultations analyzed in this study, grouped by region and the model run used for the simulations. The occultation identifier (*roid*), acquisition date and tangent-point coordinates are given for each case. PAZ identifiers are prefixed by `PAZ1`; Spire identifiers are prefixed by `FM166`, `FM167`, or `FM170`.

Occultation ID	**Date**	**Lat (°)**	**Lon (°)**	**AROME run (UTC) + forecast lead time (h)**	**ARPEGE run (UTC) + forecast lead time (h)**
France (5 cases)					
FM167.2023.129.09.22.G09	2023–05–09 09:21	51.39	4.38	2023–05–09 09h + 0h	2023–05–09 06h + 4h
FM170.2023.159.10.15.R02	2023–06–08 10:15	48.20	-6.33	2023–06–08 09h + 1h	2023–06–08 06h + 4h
FM167.2023.170.10.31.C20	2023–06–19 10:31	41.75	-2.95	2023–06–19 06h + 4h	2023–06–19 06h + 4h
PAZ1.2023.173.06.57.G11	2023–06–22 06:56	49.36	3.08	2023–06–22 06h + 1h	2023–06–22 06h + 1h
FM166.2023.190.10.03.G15	2023–07–09 10:03	48.33	3.37	2023–07–09 06h + 4h	2023–07–09 06h + 4h
Antilles (6 cases)					
FM167.2023.176.01.39.C35	2023–06–25 01:38	18.52	-52.40	2023–06–25 00h + 2h	2023–06–25 00h + 2h
FM167.2023.180.01.52.C28	2023–06–29 01:52	19.40	-60.84	2023–06–29 00h + 2h	2023–06–29 00h + 2h
FM166.2023.233.02.04.G10	2023–08–21 02:04	11.82	-63.26	2023–08–21 00h + 2h	2023–08–21 00h + 2h
PAZ1.2023.252.21.42.G18	2023–09–09 21:42	19.22	-56.84	2023–09–09 18h + 4h	2023–09–09 18h + 2h
PAZ1.2023.293.10.32.G09	2023–10–20 10:32	14.53	-55.63	2023–10–20 00h + 10h	2023–10–20 06h + 4h
PAZ1.2024.313.20.56.G02	2024–11–08 20:56	12.66	-59.53	2024–11–08 18h + 3h	2024–11–08 18h + 3h
Reunion (8 cases)					
FM167.2023.101.18.22.G29	2023–04–11 18:22	-24.13	63.44	2023–04–11 18h + 0h	2023–04–11 18 + 0h
PAZ1.2023.353.13.01.G29	2023–12–19 13:01	-19.31	60.38	2023–12–19 12h + 1h	2023–12–19 12h + 1h
PAZ1.2023.357.16.38.G22	2023–12–23 16:38	-12.21	38.39	2023–12–23 12h + 5h	2023–12–23 12h + 5h
PAZ1.2024.013.15.20.G14	2024–01–13 15:20	-18.68	54.37	2024–01–13 12h + 3h	2024–01–13 12h + 3h
PAZ1.2024.016.12.52.G18	2024–01–16 12:51	-24.44	64.84	2024–01–16 12h + 1h	2024–01–16 12h + 1h
PAZ1.2024.017.15.46.G22	2024–01–17 15:46	-17.05	47.46	2024–01–17 12h + 4h	2024–01–17 12h + 4h
PAZ1.2024.150.02.13.G17	2024–05–29 02:13	-18.92	59.20	2024–05–29 00h + 2h	2024–05–29 00h + 2h
PAZ1.2024.164.02.53.G19	2024–06–12 02:53	-8.52	54.44	2024–06–12 00h + 3h	2024–06–12 00h + 3h
Polynesia (5 cases)					
PAZ1.2023.131.16.09.G17	2023–05–11 16:09	-17.47	-145.10	2023–05–11 12h + 4h	2023–05–11 12h + 4h

https://doi.org/10.5194/egusphere-2026-4040
Preprint. Discussion started: 16 July 2026

Table A1 – *continued*

Occultation ID	**Date**	**Lat (°)**	**Lon (°)**	**AROME run (UTC) + forecast lead time (h)**	**ARPEGE run (UTC) + forecast lead time (h)**
`PAZ1.2023.261.16.41.G18`	2023–09–18 16:41	-16.05	-146.32	2023–09–18 12h + 5h	2023–09–18 12h + 5h
`PAZ1.2024.075.15.53.G30`	2024–03–15 15:53	-21.77	-150.26	2024–03–15 12h + 4h	2024–03–15 12h + 4h
`PAZ1.2024.112.16.18.G17`	2024–04–21 16:18	-18.37	-146.55	2024–04–21 12h + 4h	2024–04–21 12h + 4h
`PAZ1.2025.003.16.43.G04`	2025–01–03 16:43	-19.03	-150.21	2025–01–03 12h + 5h	2025–01–03 12h + 5h
New Caledonia (3 cases)					
`FM167.2023.082.22.53.G25`	2023–03–23 22:53	-16.80	162.87	2023–03–23 18h + 5h	2023–03–23 12h + 11h
`PAZ1.2023.150.08.10.G21`	2023–05–30 08:09	-16.43	160.73	2023–05–30 06h + 2h	2023–05–30 06h + 2h
`PAZ1.2025.006.19.01.G30`	2025–01–06 19:01	-15.71	170.47	2025–01–06 18h + 1h	2025–01–06 18h + 1h

Code availability. The radar forward operator software is publicly available at https://github.com/UMR-CNRM/operadar (Augros, 2025). This software is governed by the open-source CeCILL-C license.

Data availability. The PAZ PRO observations (https://doi.org/10.20350/digitalCSIC/16137) (Padullés et al., 2024a) are obtained from https://paz.ice.csic.es/dataAcces.php. Data are available at https://doi.org/10.20350/digitalCSIC/17140 (Padullés et al., 2025b). The raw volumetric dual-polarization radar data are publicly accessible through the AERIS platform (https://radarsmf.aeris-data.fr/description/?uuid=dea49d60-1489-458e-a8de-589d21b14ca4, Météo-France, 2026) under a education or research license.

Author contributions. AP, RP, EC, CA, DR and MB conceived the study. CA provided the operadar forward operator code, including the recent implementations of David (2026). CD provided the polarimetric radar fields from the ARAMIS network. DR provided the AROME, AROME-OM and ARPEGE forecasts. AP developed the analysis pipeline, including the interpolation of the AROME, AROME-OM and ARPEGE model fields onto the PRO ray geometry, the implementation of the PRO forward operator, and the visualisation of the results; the operadar simulations were produced by AP and CA jointly. AP prepared the original manuscript draft. AP, CA, CD, DR, MB, RP and EC contributed to the scientific discussion, the validation of the results, and the review and editing of the manuscript.

Competing interests. The authors declare that they have no conflict of interest.

https://doi.org/10.5194/egusphere-2026-4040
Preprint. Discussion started: 16 July 2026

Acknowledgements. We acknowledge Marie Mazoyer, Meryl Wilmer, Eric Basile and Sophie Marimbordes for their help.

Financial support. This publication is part of the grants RYC2021-033309-I, CNS2024-154731, and PID2024-155592OB-C22, funded by the MCIN/AEI and the European Union "NextGenerationEU/PRTR" and "ERDF A way of making Europe". This work was also partly supported by the Spanish program Unidad de Excelencia María de Maeztu CEX2020-001058-M, and by the MaX4-SOMMA-ICE. Part of the investigations at ICE-CSIC, IEEC is done under the EUMETSAT ROMSAF CDOP4. Access to Spire PRO data was granted through ESA Third Party Mission (TPM) porposal PP0098939.

https://doi.org/10.5194/egusphere-2026-4040
Preprint. Discussion started: 16 July 2026

References

Augros, C. (2025). OPERADAR (Version 1.0.0). CNRM, Météo-France, GitHub [code], https://github.com/UMR-CNRM/operadar.

Augros, C., Caumont, O., Ducrocq, V., Gaussiat, N., and Tabary, P. (2016). Comparisons between s-, c-and x-band polarimetric radar observations and convective-scale simulations of the hymex first special observing period. *Quarterly Journal of the Royal Meteorological Society*, 142:347–362.

Bouyssel, F., Berre, L., Bénichou, H., Chambon, P., Girardot, N., Guidard, V., Loo, C., Mahfouf, J.-F., Moll, P., Payan, C., and Raspaud, D. (2022). The 2020 global operational NWP data assimilation system at Météo-France. In Park, S. K. and Xu, L., editors, *Data Assimilation for Atmospheric, Oceanic and Hydrologic Applications (Vol. IV)*, pages 645–664. Springer, Cham, Switzerland.

Bowler, N. E. and Lewis, O. (2026). Experiments with a large number of gnss-ro observations through the romex collaboration in the met office nwp system. *Atmospheric Measurement Techniques*, 19(7):2479–2505.

Bringi, V. N. and Chandrasekar, V. (2001). *Polarimetric Doppler weather radar: principles and applications*. Cambridge university press.

Brousseau, P., Seity, Y., Ricard, D., and Léger, J. (2016). Improvement of the forecast of convective activity from the arome-france system. *Quarterly Journal of the Royal Meteorological Society*, 142(699):2231–2243.

Bubnová, R., Hello, G., Bénard, P., and Geleyn, J.-F. (1995). Integration of the fully elastic equations cast in the hydrostatic pressure terrain-following coordinate in the framework of the arpege/aladin nwp system. *Monthly weather review*, 123(2):515–535.

Cardellach, E., Oliveras, S., Rius, A., Tomás, S., Ao, C., Franklin, G., Iijima, B., Kuang, D., Meehan, T., Padullés, R., et al. (2019). Sensing heavy precipitation with gnss polarimetric radio occultations. *Geophysical research letters*, 46(2):1024–1031.

Cardellach, E., Padullés, R., Tomás, S., Turk, F., Ao, C., and de la Torre-Juárez, M. (2018). Probability of intense precipitation from polarimetric gnss radio occultation observations. *Quarterly Journal of the Royal Meteorological Society*, 144:206–220.

Cardellach, E., Tomás, S., Oliveras, S., Padullés, R., Rius, A., de la Torre-Juárez, M., Turk, F. J., Ao, C. O., Kursinski, E. R., Schreiner, B., et al. (2014). Sensitivity of paz leo polarimetric gnss radio-occultation experiment to precipitation events. *IEEE Transactions on Geoscience and Remote Sensing*, 53(1):190–206.

Chen, S.-Y., Kuo, Y.-H., Li, H.-W., Padullés, R., Cardellach, E., and Turk, F. J. (2025). Comparisons of polarimetric radio occultation measurements with wrf model simulation for tropical cyclones. *Atmospheric Measurement Techniques*, 18(19):5265–5280.

Combarnous, P., Martet, M., Caumont, O., and Éric Defer (2024). Assimilation of satellite lightning data in a storm-scale numerical weather prediction system using a 3d-envar data assimilation scheme. *Monthly Weather Review*, 152(2):553 – 570.

Cucurull, L., Derber, J., Treadon, R., and Purser, R. (2007). Assimilation of global positioning system radio occultation observations into ncep's global data assimilation system. *Monthly weather review*, 135(9):3174–3193.

David, C. (2026). *Improving AROME's Polarimetric Radar Simulations: Assessment of different Microphysics schemes and Radar Forward Operator options*. PhD Thesis, Toulouse 3 University - Paul Sabatier, Toulouse.

David, C., Augros, C., Vié, B., Bouttier, F., and Le Bastard, T. (2025). Improved simulation of thunderstorm characteristics and polarimetric signatures with lima two-moment microphysics in arome. *Atmospheric Measurement Techniques*, 18(15):3715–3745.

Faure, G., Chambon, P., and Brousseau, P. (2020). Operational implementation of the arome model in the tropics: Multiscale validation of rainfall forecasts. *Weather and Forecasting*, 35(2):691 – 710.

Fielding, M. D. and Janisková, M. (2020). Direct 4d-var assimilation of space-borne cloud radar reflectivity and lidar backscatter. part i: Observation operator and implementation. *Quarterly Journal of the Royal Meteorological Society*, 146(733):3877–3899.

https://doi.org/10.5194/egusphere-2026-4040
Preprint. Discussion started: 16 July 2026

Figueras i Ventura, J., Boumahmoud, A.-A., Fradon, B., Dupuy, P., and Tabary, P. (2012). Long-term monitoring of French polarimetric radar data quality and evaluation of several polarimetric quantitative precipitation estimators in ideal conditions for operational implementation at C-band. *Quarterly Journal of the Royal Meteorological Society*, 138(669):2212–2228.

Geer, A. J. (2021). Physical characteristics of frozen hydrometeors inferred with parameter estimation. *Atmospheric Measurement Techniques*, 14(8):5369–5395.

Geer, A. J., Bauer, P., Lonitz, K., Barlakas, V., Eriksson, P., Mendrok, J., Doherty, A., Hocking, J., and Chambon, P. (2021). Bulk hydrometeor optical properties for microwave and sub-millimetre radiative transfer in rttov-scatt v13.0. *Geoscientific Model Development*, 14(12):7497–7526.

Geer, A. J., Lonitz, K., Weston, P., Kazumori, M., Okamoto, K., Zhu, Y., Liu, E. H., Collard, A., Bell, W., Migliorini, S., Chambon, P., Fourrié, N., Kim, M.-J., Köpken-Watts, C., and Schraff, C. (2018). All-sky satellite data assimilation at operational weather forecasting centres. *Quarterly Journal of the Royal Meteorological Society*, 144(713):1191–1217.

Healy, S., Jupp, A., and Marquardt, C. (2005). Forecast impact experiment with gps radio occultation measurements. *Geophysical Research Letters*, 32(3).

Helmus, J. J. and Collis, S. M. (2016). The python ARM radar toolkit (py-ART), a library for working with weather radar data in the python programming language. 4(1):e25.

Hotta, D., Lonitz, K., and Healy, S. (2024). Forward operator for polarimetric radio occultation measurements. *Atmospheric Measurement Techniques*, 17(3):1075–1089.

Ikuta, Y., Okamoto, K., and Kubota, T. (2021). One-dimensional maximum-likelihood estimation for spaceborne precipitation radar data assimilation. *Quarterly Journal of the Royal Meteorological Society*, 147(735):858–875.

Kursinski, E., Hajj, G., Schofield, J., Linfield, R., and Hardy, K. R. (1997). Observing earth's atmosphere with radio occultation measurements using the global positioning system. *Journal of Geophysical Research: Atmospheres*, 102(D19):23429–23465.

Köcher, G., Zinner, T., Knote, C., Tetoni, E., Ewald, F., and Hagen, M. (2022). Evaluation of convective cloud microphysics in numerical weather prediction models with dual-wavelength polarimetric radar observations: methods and examples. *Atmospheric Measurement Techniques*, 15(4):1033–1054.

Lac, C., Chaboureau, J.-P., Masson, V., Pinty, J.-P., Tulet, P., Escobar, J., Leriche, M., Barthe, C., Aouizerats, B., Augros, C., Aumond, P., Auguste, F., Bechtold, P., Berthet, S., Bielli, S., Bosseur, F., Caumont, O., Cohard, J.-M., Colin, J., Couvreux, F., Cuxart, J., Delautier, G., Dauhut, T., Ducrocq, V., Filippi, J.-B., Gazen, D., Geoffroy, O., Gheusi, F., Honnert, R., Lafore, J.-P., Lebeaupin Brossier, C., Libois, Q., Lunet, T., Mari, C., Maric, T., Mascart, P., Mogé, M., Molinié, G., Nuissier, O., Pantillon, F., Peyrillé, P., Pergaud, J., Perraud, E., Pianezze, J., Redelsperger, J.-L., Ricard, D., Richard, E., Riette, S., Rodier, Q., Schoetter, R., Seyfried, L., Stein, J., Suhre, K., Taufour, M., Thouron, O., Turner, S., Verrelle, A., Vié, B., Visentin, F., Vionnet, V., and Wautelet, P. (2018). Overview of the Meso-NH model version 5.4 and its applications. *Geoscientific Model Development*, 11(5):1929–1969.

Lafore, J. P., Stein, J., Asencio, N., Bougeault, P., Ducrocq, V., Duron, J., Fischer, C., Héreil, P., Mascart, P., Masson, V., et al. (1998). The meso-nh atmospheric simulation system. part i: Adiabatic formulation and control simulations. In *Annales geophysicae*, volume 16, pages 90–109. Springer Verlag Göttingen, Germany.

Lopez, P. (2002). Implementation and validation of a new prognostic large-scale cloud and precipitation scheme for climate and data-assimilation purposes. *Quarterly Journal of the Royal Meteorological Society: A journal of the atmospheric sciences, applied meteorology and physical oceanography*, 128(579):229–257.

https://doi.org/10.5194/egusphere-2026-4040
Preprint. Discussion started: 16 July 2026

Mangla, R., Borderies, M., Chambon, P., Geer, A., and Hocking, J. (2025). Assessment and application of melting-layer simulations for spaceborne radars within the rttov-scatt v13.1 model. *Atmospheric Measurement Techniques*, 18(12):2751–2779.

Mishchenko, M. I. and Travis, L. D. (1994). T-matrix computations of light scattering by large spheroidal particles. *Optics Communications*, 109(1):16–21.

Morrison, H., van Lier-Walqui, M., Fridlind, A. M., Grabowski, W. W., Harrington, J. Y., Hoose, C., Korolev, A., Kumjian, M. R., Milbrandt, J. A., Pawlowska, H., Posselt, D. J., Prat, O. P., Reimel, K. J., Shima, S.-I., van Diedenhoven, B., and Xue, L. (2020). Confronting the challenge of modeling cloud and precipitation microphysics. *Journal of Advances in Modeling Earth Systems*, 12(8):e2019MS001689.

Murphy Jr, M. J., Haase, J. S., Padullés, R., Chen, S.-H., and Morris, M. A. (2019). The potential for discriminating microphysical processes in numerical weather forecasts using airborne polarimetric radio occultations. *Remote Sensing*, 11(19):2268.

Padullés, R., Cardellach, E., and Oliveras, S. (2024a). resprf [dataset].

Padullés, R., Cardellach, E., Paz, A., and Burger, T. (2025a). Initial polarimetric radio occultation results from spire's nanosatellite constellation: Independent assessment and potential applications. *Bulletin of the American Meteorological Society*, 106(4):E735–E751.

Padullés, R., Cardellach, E., Paz, A., Oliveras, S., Hunt, D. C., Sokolovskiy, S., Weiss, J. P., Wang, K.-N., Turk, F. J., Ao, C. O., et al. (2024b). The paz polarimetric radio occultation research dataset for scientific applications. *Earth System Science Data Discussions*, 2024:1–28.

Padullés, R., Cardellach, E., Paz, A., and Turk, F. (2025b). Scattering amplitude matrix co-polar components for gnss polarimetric radio occultations observation geometry, digital. csi [data set]. *CSI [data set]*, 10.

Padullés, R., Cardellach, E., Paz, A., and Turk, F. J. (2025c). Polarimetric radio occultation forward scattering sensitivity to hydrometeor habit. *Geophysical Research Letters*, 52(14):e2025GL115757.

Padullés, R., Cardellach, E., Turk, F. J., Ao, C. O., de la Torre Juárez, M., Gong, J., and Wu, D. L. (2021). Sensing horizontally oriented frozen particles with polarimetric radio occultations aboard paz: Validation using gmi coincident observations and cloudsat a priori information. *IEEE Transactions on Geoscience and Remote Sensing*, 60:1–13.

Paz, A., Lonitz, K., Padullés, R., and Cardellach, E. (2026). Development and evaluation of a hydrometeor-dependent forward operator for polarimetric radio occultations in the ifs: application to atmospheric rivers. *Journal of Advances in Modeling Earth Systems (under review)*.

Paz, A., Padullés, R., and Cardellach, E. (2024). Evaluating the polarimetric radio occultation technique using nexrad weather radars. *Remote Sensing*, 16(7):1118.

Paz, A., Padullés, R., and Cardellach, E. (2025). Constraining microphysics assumptions on the modeling of atmospheric rivers using gnss polarimetric radio occultations. *Atmospheric Chemistry and Physics*, 25(23):17797–17817.

Pinty, J.-P. and Jabouille, P. (1998). A mixed-phase cloud parameterization for use in a mesoscale non-hydrostatic model: Simulations of a squall line of orographic precipitation. *American Meteorological Society, Everett, WA*, pages 217–220.

Ruston, B. and Healy, S. (2021). Forecast impact of FORMOSAT-7/COSMIC-2 GNSS radio occultation measurements. *Atmospheric Science Letters*, 22(3):e1019.

Ryzhkov, A. V. and Zrnić, D. S. (2019). *Radar polarimetry for weather observations*, volume 486. Springer.

Schrom, R. S. and Kumjian, M. R. (2018). Bulk-density representations of branched planar ice crystals: Errors in the polarimetric radar variables. *Journal of Applied Meteorology and Climatology*, 57(2):333–346.

Seity, Y., Brousseau, P., Malardel, S., Hello, G., Bénard, P., Bouttier, F., Lac, C., and Masson, V. (2011). The AROME-France convective-scale operational model. *Monthly Weather Review*, 139(3):976–991.

https://doi.org/10.5194/egusphere-2026-4040
Preprint. Discussion started: 16 July 2026

Shrestha, P., Trömel, S., Evaristo, R., and Simmer, C. (2022). Evaluation of modelled summertime convective storms using polarimetric radar observations. *Atmospheric Chemistry and Physics*, 22(11):7593–7618.

Talpe, M. J., Nguyen, V. A., and Tomás, S. (2025). Initial polarimetric radio occultation results from spire's nanosatellite constellation: Satellite payload, collection, and calibration. *Bulletin of the American Meteorological Society*, 106(4):E714–E734.

Tiedtke, M. (1989). A comprehensive mass flux scheme for cumulus parameterization in large-scale models. *Monthly weather review*, 117(8):1779–1800.

Trömel, S., Blahak, U., Evaristo, R., Mendrok, J., Neef, L., Pejcic, V., Scharbach, T., Shrestha, P., and Simmer, C. (2023). Fusion of radar polarimetry and atmospheric modeling. IET.